Predictability of the Seasonal Mean Atmospheric Circulation During Autumn, Winter, and Spring

David Straus, Dan Paolino and J. Shukla
Center for Ocean-Land-Atmosphere Studies

Siegfried Schubert and Max Suarez
NASA - Goddard Space Flight Center

Arun Kumar
National Centers for Environmental Prediction

Philip Pegion
Science Applications International Corporation

Corresponding author address:
David M. Straus
4041 Powder Mill Rd., Suite 302
Calverton, MD 20705

email: straus@cola.iges.org
September 10, 2002

Abstract.

The predictability of the autumn, boreal winter, and spring seasons with foreknowledge of sea surface temperatures (SSTs) is studied using ensembles of seasonal simulations of three General Circulation Models (GCMs): the Center for Ocean-Land-Atmosphere Studies (COLA) GCM, the National Aeronautics and Space Administration Seasonal to Interannual Prediction Project (NSIPP) GCM, and the National Centers for Environmental Prediction (NCEP) GCM. Warm-minus-cold composites of the ensemble mean and observed tropical Pacific precipitation, averaged for the three warmest El Niño and three coldest La Niña winters, show large positive anomalies near the dateline, which extend eastward to the South American coast. The same is true for composites of the spring following the event. In the composites of the autumn preceding the event, the precipitation is weaker and shifted off the equator in the far eastern Pacific, where equatorial SSTs are too low to support convection. The corresponding boreal winter 200 hPa height composites show strong signals in the tropics and midlatitudes of both hemispheres. The subsequent spring composites are similar, but weaker in the northern extra tropics. In the preceding autumn composites, the overall height signal is quite weak, except in the southern Pacific.

The model dependence of the signal (variance of ensemble means) and noise (variance about the ensemble means) of the seasonal mean 200 hPa height is small, a result that holds for all three seasons and is in contrast to earlier studies. The signal to noise ratio is significantly greater than unity in the tropics (all seasons), the northern Pacific and continental North America subtropics (boreal winter and spring), and the southern Pacific subtropics (boreal autumn).

Rotated empirical orthogonal function analysis of the tropical Pacific SST recovers El Niño - like dominant patterns in boreal winter and spring, but emphasizes two SST patterns in autumn, one with largest SST in the far eastern tropical Pacific, and one a maximum nearer the dateline. Two methods are used to assess the precipitation and height field responses to these patterns: linear regression of the ensemble means on the principal component (PC) time series of SST and identication of patterns that optimize the signal-to-noise ratio. The two methods yield remarkably similar results.

The optimal height patterns for boreal winter and spring are similar, although the spring response over the northern extra tropics is somewhat weaker, and some subtle changes in phase are found in all three GCMs. The associated optimal time series have serial correlations with the leading PC of SST which exceed 0.9 for all GCMs for winter and spring. For autumn the time series of the leading two optimal patterns each has a serial correlation with the corresponding PC of SST which exceeds 0.7 for the COLA and NSIPP GCMs. The autumn 200 hPa height leading optimal pattern (response to eastern Pacific SST) is quite weak, representing nearly uniform tropical warming. The second optimal pattern (response to central Pacific SST) shows a robust wave train in the southern Pacific, with a consistent belt of low height over northern midlatitudes.

1. Introduction. Boundary forced predictability on the seasonal time scale depends in a direct way on the extent to which the boundary condition anomalies, primarily tropical sea surface temperature (SST), produce strong anomalous atmospheric heat and momentum sources. Enhanced predictability in midlatitudes is only realized if the remote circulation forced by these heat and momentum sources is strong enough and consistent enough to be distinguishable from the chaotic internal variability (sometimes called noise) of the midlatitude atmosphere. The presence of this internal variability can lead to substantial uncertainty in the expected seasonal mean even in the presence of large boundary anomalies.

The need to understand the characteristics of this variability, and to learn how to distinguish it from the response forced by the boundary, has motivated a great deal of recent general circulation model (GCM) based research (Straus and Shukla, 2000, 2002; Schubert et al., 2001; Shukla et al., 2000a,b; Chang et al., 2000; Branković and Palmer, 2000; Kumar et al., 2000, for example). General circulation models (GCMs) are particularly useful in this regard, since they can provide estimates of the signal and the noise via an ensemble of seasonal solutions generated with identical boundary conditions of SST, but with different initial conditions. The disadvantage of using GCMs is of course that the signal and noise estimates are likely to be model dependent and may not be accurate. Exploring this dependence is one of the goals of Dynamical Seasonal Prediction (DSP) project (Shukla et al., 2000a), a multi-institutional cooperation aimed at better understanding seasonal predictability. (The July 2000 Part B issue of the Quarterly Journal of the Royal Meteorological Society was devoted to the DSP project and its European equivalent, the PROVOST project.) Recently,

other authors have also recognized the importance of exploring the model dependence of predictability estimates (Hoerling et al., 2001, for example).

Traditionally, research on SST-forced seasonal predictability has focused on boreal winter, when the tropical Pacific SST anomalies associated with ENSO (the El Niño Southern Oscillation) episodes are strong, the radiative forcing of the general circulation is nearly constant, and the response in the northern extra tropics well defined. Recent work on the response to ENSO during other times of the year has suggested that the early (boreal) spring response is distinguishable from the noise, but that during summer and autumn the signal is much weaker (Branković and Palmer, 1997, 2000; Kumar and Hoerling, 1998; Livezey et al., 1997). Schubert et al. (2002)(hereafter S2) do show that during summer the concomitant reduction in noise leads to signal-to-noise ratios that are comparable to those found for winter.

The purpose of this paper is to systematically explore and compare characteristics of the SST-forced signal and the associated noise in boreal autumn, winter, and spring, utilizing ensemble simulations made with three GCMs. We compare the signal patterns which optimize the signal to noise ratio for the three GCMs, and relate them to different patterns of tropical SST forcing. The optimal patterns depend on the complete set of ensemble simulations, not just the ensemble mean. The ability to access these patterns is a second attraction of using GCM ensemble simulations. Comparison of these optimal patterns among GCMs for tropical SST forcing has not previously appeared in the literature.

This paper extends previous DSP intermodel comparison studies from the winter season to the transition seasons in a unified framework. Ensembles of seasonal simulations of the

three GCMs we study (see Table 1) were generated for the boreal autumns and springs for the 18 years 1981-1998, using the same observed SSTs (Reynolds and Smith, 1994) and realistic initial conditions. In order to facilitate comparison of the transition season results with the boreal winter season, we have also run winter cases using the calendar years of 1981/82 - 1998/99 for the same three GCMs. (See section 2 for further details of the GCMs.) The winter results will help to put the transition seasons in context.

We find that in boreal spring, as in winter, large eastern tropical Pacific SST anomalies force a significant and realistic signal in the tropical Pacific and in both the northern and southern extratropics. The signal in boreal autumn is much weaker, however. In order to highlight the seasonal differences in a familiar context, we show time series of the pattern correlation of 200 hPa height between the ensemble (seasonal) mean anomaly of each GCM and the seasonal mean anomaly from observations (Figure 1). The pattern correlation is taken over the Pacific North-America region ($15^oN - 70^oN$, $180^oW - 60^oW$). The years are presented (from left to right) in order of increasing absolute value of the Niño-3 index, with red (blue) indicating El Niño (La Niña) years. The three bars shown for each year indicate the result for the three GCMs (always in the same order). For the winter season (middle panel), both the strength and consistency of the GCM pattern correlations are strongly related to the magnitude of the Niño-3 index (Shukla et al., 2000a), and this is true to some extent for the boreal spring season (shown in the bottom panel). However, the boreal autumn (top panel) shows much less skill and consistency.

These results, however, are based solely on the Niño-3 index. To explore the boundary

forcing more systematically, we analyze the near global ($50^oS - 50^oN$) SST anomalies to obtain the dominant patterns of variability, and extract the response to these anomalies from the ensemble GCM simulations. Section 2 describes both the GCMs and observations used, the SST boundary forcing, and the ensembles of seasonal simulations. Section 3 describes a composite analysis of mean precipitation and 200 hPa height based on strong El-Niño and La-Niña episodes for autumn, winter and spring seasons. Estimates of the signal and noise variance in precipitation and in 200 hPa height obtained from the different ensembles are discussed in Section 4. A nearly global pattern analysis of the SST anomalies is presented in Section 5, along with the associated tropical precipitation response. The global height response of the GCM ensemble means to these patterns (obtained by linear regression) is shown in Section 6. A separate analysis of the height patterns that optimize a suitably defined signal-to-noise ratio is presented in Section 7. A synthesis and the conclusions are presented in Section 8.

2. GCM Experiments and Data.

(a) GCMs. The three GCMs utilized are those of the Center for Ocean-Land- Atmosphere Studies (COLA), the National Aeronautics and Space Administration Seasonal to Interannual Prediction Project (NSIPP), and the National Centers for Environmental Prediction (NCEP). The models are described in more detail in subsections (d)-(f). Some overall characteristics are given in Table 1.

(b) Observed data. The SST used in all GCM simulations, and for the diagnostics in this paper, are the OISST of Reynolds (see Reynolds and Smith 1994). The COLA GCM

utilizes the SST data on a weekly basis, while the NSIPP and NCEP GCMs use the monthly SST data. All diagnostics presented use only seasonal means. The observed seasonal mean precipitation is obtained from the Xie-Arkin dataset (Xie and Arkin, 1997), while the seasonal mean 200 hPa geopotential heights are obtained from the NCEP reanalysis (Kalnay and coauthors, 1996).

(c) Simulations. The boreal autumn simulations were initialized in August and were run through the end of November for the years 1981-1998. The number of ensemble members for each GCM is given in Table 1, and the details of the initial conditions are given in subsections (d)-(f). The boreal winter simulations were initialized in November for the years 1981-1998 and were run through the following March. The boreal spring runs were initialized in February of the years 1982-1999 and run through June.

(d) COLA GCM. This GCM is Version 2.2 of the COLA GCM, run at horizontal spectral resolution of triangular T63, with 18 sigma levels. It uses the dynamical core of the National Center for Atmospheric Research Center Community Model version 3 (CCM3) described in Kiehl et al. (1998); otherwise it is as described in Schneider (2002). The dependent variables of the model are spectrally treated, except the moisture variable, which is advected using the semi-Lagrangian technique. The land surface model (LSM), which is coupled to the atmospheric model, is the Simplified Biosphere Model (SSiB) documented in Xue et al. (1991). The parameterization of deep convection is the relaxed Arakawa- Schubert scheme (Moorthi and Suarez, 1992). For further details consult Schneider (2002).

There are 10 members in each ensemble. Initial conditions (ICs) 1-5 for the boreal autumn

runs are obtained from NCEP reanalyses for 00 UTC on the last five days of August. Initial conditions 6-10 were obtained from ICs 1-5 by adding a perturbation which consists of the difference between the analyses 12 hours after and 12 hours before. The initial conditions for the boreal winter (spring) runs were obtained in the same manner utilizing the reanalyses for the last five days of November (February). The land surface initial conditions were taken from a climatology compatible with SSiB.

(e) NSIPP GCM. This GCM is the NSIPP-1 AGCM. It uses the grid-point 4th-order dynamical core of Suarez and Takacs (1995), and was run with a horizontal resolution of 2^o latitude by 2.5^o longitude, and with 34 vertical sigma levels. The parameterization of deep convection is the relaxed Arakawa-Schubert scheme (Moorthi and Suarez, 1992). For further details consult Bacmeister and Suarez (2002). The atmospheric model is coupled to the Mosaic LSM described by Koster and Suarez (1992).

There are 9 members in each ensemble. Initial conditions (ICs) for the boreal autumn runs were obtained from the NCEP reanalyses from 00 UTC of August 13-17, and from 12 UTC of August 13-16. The ICs for the boreal winter (spring) runs were obtained in the same manner utilizing the reanalyses for November (February) 13-17. The land surface initial condition for each ensemble member and for all years of the boreal winter runs was taken from an arbitrary December state from a previous experiment. Simulations for the boreal autumn and spring seasons took the land surface IC from a previous multi-year continuous simulation made with observed SSTs, using the corresponding month and year. (Thus for the autumn and spring runs, the land initial states can potentially contribute to the forecast

skill indirectly through the SST that forced the previous runs.)

(f) NCEP GCM. This GCM is the NCEP Seasonal Forecast Model (Kanamitsu et al., 2002). The model is a spectral model with triangular resolution of T62, with 28 sigma levels in the vertical. It utilizes the same parameterization of deep convection as the COLA and NSIPP GCMs. The land processes are represented by the two-layer LSM of Pan and Mahrt (1987). Further details are given in Kanamitsu et al. (2002).

There are 10 members in each ensemble. Initial conditions (ICs) for the boreal autumn runs were obtained from the NCEP reanalyses from 00 UTC and 12 UTC of September 1-5. The ICs for the boreal winter (spring) runs were obtained in the same manner utilizing the reanalyses for November (February) 1-5. The land surface conditions were taken from a climatology compatible with the land surface model.

3. The ENSO-Related Global Signal Composite seasonal means for the boreal autumn, winter, and spring seasons based on the traditional wintertime ENSO framework serve as a useful reference. The three winters with the highest values of Niño-3[1] (JFM 1983, 1998, 1992) are defined as warm winters, while those with the lowest values of Niño-3 (JFM 1989, 1985, 1999) are defined as cold winters. (See Figure 1). The autumns preceding these winters and the springs following them are considered to be part of the three warm and three cold episodes, even though they do not necessarily have the largest magnitude of Niño-3. Subtracting the average of a seasonal mean field over the three cold episodes from the average

[1]Niño-3 is defined as the SST anomaly averaged over the area $150^oW - 90^oW, 5^oS - 5^oN$, and is obtained from the data of Smith et al. (1996).

of that field over the three warm episodes gives a simple composite measure of the warm minus cold anomalies.

The composite SST warm-minus-cold differences are shown by the contours in Figure 2, while the shading indicates regions where the winter-averaged SST for the warm events exceeds 28^oC, giving a rough indication of where conditions are favorable for convective activity. While autumn (Figure 2a) SST anomalies are as large as during winter over much of the eastern Pacific, the temperature along the equator in autumn east of 135^oW is too low to support convection even in the warm years. Conversely, while the spring anomalies over much of the eastern equatorial Pacific are smaller than their winter counterparts, the water is warm enough to support convection along the equator right up to the South American coast. Here the winter (spring) anomalies exceed 3^o (4^o).

Figure 3 shows the corresponding differences for the observed precipitation over the tropical Pacific basin. The winter anomaly (middle panel) shows the familiar ENSO signal, with largest positive anomalies just east of the dateline and an eastward extension along the equator right up to the coast of South America. The springtime precipitation anomaly (bottom panel) is very similar in structure to that in the preceding winter, with a somewhat reduced magnitude in the central Pacific. The equatorial anomalies in the eastern Pacific are just as strong as in winter. In contrast, the preceding autumn's composite anomaly (top panel) is considerably weaker east of 120^oW, especially along the equator, consistent with the position of the 28^oC isotherm in Figure 2. The autumn anomalies near the dateline are as strong as in spring. In all seasons, negative anomalies are seen poleward of about 10^o in

both hemispheres in the central Pacific and in the western Pacific.

The corresponding GCM seasonal-mean, warm-minus-cold precipitation anomalies are shown in Figure 4. Here we have averaged the seasonal-mean composites over all members of the ensembles and over the three GCMs. The main conclusions gleaned from the observations are unchanged: the spring warm-minus-cold composite is as strong in the eastern Pacific along the equator as in winter, while the autumn composite difference is smaller here. However, the GCMs do show a stronger than observed precipitation anomaly in the central Pacific during spring than during autumn.

The warm-minus-cold composites for the global 200 hPa height field obtained from reanalyses are shown in Figure 5. The winter warm-minus-cold composite shows the expected dramatic warming in the tropical Pacific, the well-known ENSO response pattern over the Pacific North American (Pac-NA) region (see for example, Straus and Shukla 2000, 2002), and a quite well-defined wave train in the Southern Hemisphere. In addition, a high latitude dipole over the North Atlantic region and a mid-latitude dipole over East Asia are seen. The following spring height composites contain the same basic structures, although with a reduced magnitude and with a distinct shift in the enhanced Aleutian Low. The anomalies over the Pac-NA region nearly disappear in the preceding autumn, although the Southern Hemisphere response and the dipoles over the North Atlantic and East Asia are discernible. The GCM composite 200 hPa height response is shown in Figure 6, averaged as before over the ensembles of all three GCMs. The main tropical, Pac-NA region and Southern Hemisphere observed features are all clearly seen in the mean GCM results, as well as the low over

subtropical East Asia. During spring, the high over North America is more distinct than in observations, and is shifted to the west compared to nature. The high latitude dipole and the highs over mid-latitude East Asia are missing, suggesting that they are due to climate noise. The zonally symmetric anomalies suggested by the observations and found even more clearly in the GCM results have been pointed out before (Hoerling et al., 1995).

These preliminary results suggest that while the spring looks in some sense like a weaker version of winter (with some of the Northern Hemisphere features shifted), the autumn response to tropical SST forcing is fundamentally different. While this ENSO oriented analysis derived from the Niño-3 index is useful, the weak autumn response suggests we should look to other tropical SST anomaly signals.

4. Signal and Noise Variance. A major benefit of GCM simulations in the study of seasonal predictability is the ability to separate the forced SST response from the variability of the seasonal mean due to internal chaotic dynamics. The overall level of internal variability (the noise variance) can be estimated from the average intra-ensemble variance, while a measure of the SST forced signal is the temporal variance of the ensemble mean, corrected for the presence of noise (see Scheffé 1959, p225; also Rowell et al. 1995; Straus and Shukla 2000). The panels in Figure 7 show the signal variance of seasonal mean 200 hPa height, the internal (noise) variance, and their ratio for the three GCMs for boreal autumn. The signal variance (shown in panels (a)-(c)) consistently shows a large signal in the Southern Hemisphere and a smaller signal over the Pacific and East Asia in all three GCMs. The signal over North America is very weak. The noise variance (shown in panels (d)-(f)) is also

consistently large in these same regions, leading to a generally weak signal-to-noise ratio outside the tropics in all three GCMs. This dimensionless ratio is shown in panels (g)-(i). Significance at the 95% (99%) levels is shown by the light (dark) shading. The significance test we use refers to rejecting the null hypothesis that the signal to noise ratio $r \leq 1$, which leads to a stricter test than that commonly used (null hypothesis $r = 0$). See Scheffé (1959, pg. 227) for the calculation of significance. Outside the tropics, only the subtropical southern Pacific shows a ratio which is significant.

The corresponding results for boreal spring are shown in Figure 9. All three GCMs have strong signals in the Pacific and over North America, in the Southern Pacific, and even in the tropics, the latter reflecting the overall warming of the tropics during warm events. Again, the noise tends to be strongest where the signal is strongest, but now the ratio is significantly larger than 1.0 over subtropical North America, and for the NCEP GCM over the mid-latitude Pacific as well. As before, highly significant ratios are seen over the tropics, indicating very little noise there.

The autumn and spring results should be put in the context of the boreal winter variances given in Figure 8. (Note the differences in the contours used.) The winter signal variances are stronger than either transition season, with the large signals over the Pac-NA region dominating the tropics and Southern Hemisphere. The North Pacific is also a region of large noise (particular in the COLA GCM), yet the ratio is still significantly greater than 1.0 in the northeast Pacific and over the subtropical North American continent.

Some model dependence to the signal and noise variances can be seen in Figures 7 - 9. In

particular the COLA GCM tends to have a larger noise variance, especially over the Pacific during winter. Yet the discrepancies are in general less than those shown for an earlier generation of models used in Shukla et al. (2000a) indicating some convergence may have been achieved. We return to this point in the discussion.

5. SST patterns. In order to objectively organize the dominant seasonal mean patterns of SST forcing anomalies, we have performed a rotated empirical orthogonal rotation (REOF) analysis of the near global ($50^oS - 50^oN$) SST anomalies, using the same SST data which forced the GCMs (see section 2). For boreal winter and spring there is a large difference in the cumulative globally averaged temporal variance explained by the first two REOF patterns, with the leading REOF associated with about three times the variance of REOF-2 (see Table 2). In boreal autumn the variances explained by the leading two REOFs are closer (31% vs. 19%), and so we consider both modes. Figure 10 shows these two REOF patterns, as well as the leading REOF patterns for winter and spring. REOF-1 for all three seasons is dominated by warming in the eastern Pacific, with the winter pattern corresponding to the classical ENSO signal, and the spring and fall leading REOFs having a maximum just off the South American coast. This large eastern tropical Pacific weighting leads naturally to large correlation with the Niño-3 index (see Table 3), and the corresponding time series (principal components, or PCs) generally have peaks during the strong ENSO episodes of fall/winter/spring 1982/83, 1986/87, 1988/89, 1991/92, and 1997/98 (see Figure 11). The second REOF pattern for autumn has a broad maximum in the central Pacific, and a strong positive anomaly in the North Pacific. Its time series is not well correlated with Niño-3,

nor does it have peaks for the autumns preceding the largest ENSO events (Figure 11, top panel). Since the warmest waters are generally confined to the central Pacific during autumn (as seen in Figure 2), this mode of SST anomaly is expected to be important for forcing an atmospheric response. The two patterns shown for autumn here are quite similar to those shown by S2 for boreal summer (their Figure 6).

6. Response of Precipitation. The linear response of seasonal mean precipitation to the dominant pattern of SST during JFM and MAM is obtained by linear regression of this field on the associated PC of SST. For the GCMs, this regression is done using the ensemble mean. The results (not shown) are consistent with the warm minus cold composites seen in Figures 3 and 4. The two seasons show a similar response dominated by positive anomalies over the central and eastern equatorial Pacific (and negative anomalies surround this to the north, south, and west, in a characteristic "horseshoe" shape). The peak magnitude of the boreal spring response is somewhat smaller than in winter, again consistent with the composites.

The linear response of the ensemble mean precipitation to the two leading autumn SST patterns is estimated by regression of the means on PC-1 and PC-2, as shown in Figures 12 and 13 for the observations and all three GCMs. The regression on PC-1 is similar to the Niño-3 composites shown earlier, with a dominant central Pacific positive anomaly that weakens and extends towards the South American coast. The regression on PC-2 has some similarity to that for PC-1, but the dominant positive anomaly in the tropical Pacific is more closely confined near the dateline. Also, all three GCMs show a strong negative anomaly in

the western Pacific north of the equator.

By using regression of the GCM ensemble mean on the seasonal-mean SST to assess the forced signal, we are making the assumptions that the signal depends only the seasonal mean of the SST, and that this dependence is linear. For example, Straus and Shukla (2002) argue that the midlatitude height signal is more linearly related to the tropical diabatic heating than to the SST. In order to confirm that the results obtained by the regression method are not very sensitive to these assumptions, we also use an alternate approach to finding the dominant forced signal. In this method, which is equivalent to the signal detection technique discussed in Venzke et al. (1999), the GCM seasonal means from all ensemble members are used to find a set of patterns, ordered by the magnitude of the signal-to-noise ratio. For each pattern, the signal is defined as the temporal variance of the ensemble mean of the time series associated with that pattern, and the noise is defined as the average intra-ensemble variance of the time series (see the Appendix for details). This method utilizes all ensemble members, not just the ensemble mean, and makes no assumptions about what the appropriate forcing field or time-scale is. By comparing the results of these two methods, with their distinct approaches to the estimation of the forced signal, we aim to assess the reliability of the results.

The two leading optimal patterns for precipitation are shown for all three GCMs for boreal autumn in Figures 14 and 15. Comparing Figure 14 with Figure 12, and Figure 15 with Figure 13, one sees that the patterns deduced from linear regression on the SST time series are extremely well-reproduced by the leading optimal patterns, although the overall

magnitude of the response is not always the same for the two methods. This suggests that the tropical responses to the leading two leading modes of SST are, in fact, distinct.

7. Response of Global Height. The patterns which optimize the signal to noise ratio give an estimate of the GCM ensemble response to prescribed SST forcing that does not assume the response is linear in the forcing, and which takes into account the climate noise given by the ensemble spread. Figures 16 and 17 show the leading optimal pattern for boreal winter and spring, respectively, for the three GCMs for seasonal mean 200 hPa height. The models all show the expected tropical warming (particularly in the eastern Pacific) for both seasons, and well-defined wave trains in both hemispheres in the 180^oE to 300^oE longitude belt. The spring pattern for each GCM is very similar in structure to the corresponding winter pattern, but with a smaller amplitude and with systematic shifts in northern midlatitudes. The winter maps in the Pacific North American region look very similar to the ENSO-related pattern familiar from recent literature (see for example Straus and Shukla 2000, 2002 for maps and references). The enhanced Aleutian Low, the subtropical low over continental North America, and the high over northeastern Canada are present in all maps. In general the COLA and NSIPP GCM's responses are very similar; the NCEP GCM differs in producing a weaker and slightly displaced Canadian high, and a quite strong and broad subtropical response over Asia. Not only do all the models show a weaker response in spring than in winter, but both the low over the North Pacific and the Canadian high are shifted westward consistently in the models.

In order to determine whether these optimal patterns are consistent with the assumption

of linearity with respect to the forcing, we computed the serial correlation coefficient of the time series associated with the leading optimal pattern with the PC of the first rotated EOF of SST for boreal winter and spring (Figure 11). The results (see Table 4) show very high values of the correlation (exceeding 0.90 in all cases), indicating that these patterns can to a good approximation be thought of as linear responses to the SST forcing patterns represented in Figures 11c and 11d. As would be expected, the linear regression of the ensemble mean height fields on the leading SST PC for winter and spring (not shown) yield patterns very similar to those shown in Figures 16 and 17.

The results for boreal autumn are quite different. The leading two optimal modes are shown for all GCMs in Figures 18 and 19. The leading optimal mode has very weak features (note the contour interval in Figure 18). For the COLA and NSIPP GCMs a nearly uniform tropical warming dominates, with a remnant of some of the midlatitude winter and spring features appearing. The NCEP GCM shows a nearly uniform global warming. The second optimal pattern, defined as the pattern which optimizes the signal to noise ratio subject to the constraint that it is independent of the first pattern, bears some similarity to the boreal spring responses. In particular, the enhanced Aleutian Low, along with its extension westward into East Asia, is seen in all GCMs, and even a weak eastward extension across southern North America is noted in the COLA and NSIPP responses. The Southern Hemisphere wave trains are stronger than in either winter or spring, and are slightly shifted both westward and towards the equator.

The interpretation of each of these patterns in terms of SST forcing is facilitated by the

hypothesis that each is linearly related to the corresponding SST rotated EOF. The correlation coefficients for both modes shown in Table 4 give some support for this hypothesis, more so for the COLA and NSIPP GCMs than for the NCEP GCM. The notion that only a generalized warming (or cooling) of the tropical belt is forced by the leading SST pattern is consistent with Figure 2, which implies that strong regional convective forcing in the eastern Pacific cannot be effective on the seasonal-mean time scale. This convective forcing does occur in the central Pacific (as in the second SST pattern), and leads to wave trains in both hemispheres. While the particularly strong central Pacific wave train in the Southern Hemisphere (during austral spring) is interesting as an example of a forced stationary response, it also may have some practical value for seasonal forecasts over New Zealand. The secondary wave train in the western Pacific south of the equator seen in the COLA GCM is presumably related to the equatorial anomalies of precipitation seen in Figure 13.

It is noteworthy that the boreal autumn height response seen here bears some similarity to ensemble GCM results obtained for summer using the NSIPP-1 GCM (see S2). As mentioned earlier, the leading two EOFs of SST shown in S2 (their Figure 6) bear a strong similarity to Figures 10a and 10b: the leading EOF is dominated by warm SST in the far eastern tropical Pacific, with some Indian Ocean signal, while the second EOF shows the dominant warming in the central Pacific. The boreal summer mean 200 hPa height responses obtained by S2 using linear regression on the SST PCs (and shown in their Figure 9) bears some similarity to Figures 18 and 19. The nearly uniform tropical warming seen in the leading pattern, and the Southern Hemisphere wave trains and Northern Hemisphere lows seen in the Pacific, Asia

and even over the Atlantic in the second optimal pattern are all seen in the corresponding regression results of S2. However, the zonally symmetric nature of the summer response in S2 is less evident in the autumn optimal patterns.

8. Summary and Conclusions. The characteristics of the seasonal mean response forced by global SST boundary conditions are difficult to estimate directly from observations because of the large noise component arising from non-linear, chaotic dynamics. The use of ensembles of GCM simulations allows us in principle to obtain separate estimates of the true boundary forced signal and the noise. This becomes particularly important during the transition seasons when the signal is smaller than in winter. In this study we have extended the Dynamical Seasonal Prediction project (Shukla et al., 2000a) by focusing on the transition seasons. We have, in particular, examined the forced response, the noise variance, and their model dependence utilizing ensemble seasonal simulations from three GCMs. The optimal signal to noise patterns, used here for the first time to compare GCM results, make use of the entire probability distribution of the ensemble, not just the ensemble mean.

The signal and noise variances of the GCMs for seasonal mean-200 hPa heights are generally similar to each other and do not display the striking differences seen in earlier studies (e.g. Shukla et al. 2000a). The warm-minus-cold composite precipitation and height fields for the boreal springs following the large winter events show patterns generally similar to those for winter, both in the ensemble mean GCM results and in observations. In particular, the equatorial eastern Pacific precipitation anomalies have similar magnitudes in winter and spring. However, the composites using the boreal autumns preceding the large

winter events show much weaker global height responses, and an equatorial precipitation signal that is much weaker in the eastern Pacific, corresponding to the complete absence of water warm enough to excite convection. These findings suggest that the winter ENSO response paradigm of a wave train extending from the subtropical Pacific to North America is more applicable to boreal spring than to boreal autumn.

This suggestion is strengthened by a fuller analysis of both the tropical SST patterns and the global height response. The evolution of the pattern which has the largest signal to noise ratio for 200 hPa height is highly correlated with the PC time series of the leading SST REOF pattern for both boreal spring and winter, and for all three GCMs. Since the optimum analysis of the height field does not assume linearity with respect to forcing, these results suggest that, to leading order, the signal defined from optimal analysis is in fact linear in SST.

During boreal autumn, two modes of SST variability and two global height signals emerge. The eastern tropical Pacific SST variability excites a general (weak) tropical warming, but cannot excite well-defined wave trains as in the other seasons because of the lack of warm water in the eastern Pacific even during warm events. The SST pattern which strongly weights the central equatorial Pacific is correlated at about the 0.70 level with a height response showing both an intense wave train in the Southern Hemisphere and more modest and more zonally symmetric features in the Northern Hemisphere. Strong similarities with the summer season behavior found by S2 were noted

The ensemble simulations of the three GCMs utilized agree reasonably well with each

other in terms of the overall level of signal and noise, and on the forced signals and their relationship to the dominant SST patterns in boreal spring and autumn. Spring appears much closer to winter, with the dominant signal related to the eastern tropical Pacific warm SST events via enhanced tropical convection there. The relatively weak mid-latitude signals in autumn, on the other hand, appear more closely related to warming and enhanced convection in the central Pacific.

A caveat in this study relates to an important similarity of the three GCMs. All three GCMs use very similar versions of the relaxed Arakawa-Schubert convection parameterization. Since this parameterization is centrally involved in converting the SST anomaly provided as a boundary condition into a deep tropical convective heat source, its behavior may have a strong effect on the simulation of the forced response. Further GCM comparisons, encompassing a wider suite of model parameterizations, are needed.

The success of the technique used provides a framework for posing further dynamical questions related to the transition season signals. For example, what are the roles of the transients and of the propagation characteristics of the mean three- dimensional circulation in modulating the tropical forced signals? How important are intra-seasonal variations in SST in altering the signals?

Acknowledgements. We are indebted to Dr. T. DelSole for introducing us to the optimal pattern technique, and for providing us with the relevant computer programs. This work was supported by the National Science Foundation under grant ATM-98-14295, the National Aeronautics and Space Administration (NASA) under grant NAG5-8 208, and

the National Oceanic and Atmospheric Administration (NOAA) under grant NA96-GP0056. We also wish to gratefully acknowledge the support of the NASA Seasonal to Interannual Prediction Project, and of NOAA's Climate Diagnostics and Experimental Prediction Program.

GCM	Resolution	L	N	Reference
COLA	T63	18	10	Schneider (2002)
NSIPP	2.0 x 2.5	34	9	Bacmeister and Suarez (2002)
NCEP	T62	28	10	Kanamitsu et al. (2002)

Table 1: Summary of GCMs, showing horizontal resolution in triangular truncation for spectral models, latitude by longitude resolution for the grid point model, number of vertical levels L, and number of ensemble members N.

Season	Mode n	PctVar
SON	1	31.3
SON	2	19.3
JFM	1	33.1
JFM	2	9.4
MAM	1	28.5
MAM	2	11.8

Table 2: Percentage of total variance associated with rotated EOFs of SST, labelled as PctVar.

Season	Mode n	Corr
SON	1	0.93
SON	2	0.34
JFM	1	0.98
MAM	1	0.91

Table 3: Correlation between the SST PC associated with rotated EOF mode n and the Niño-3 index.

Season	Mode n	COLA	NSIPP	NCEP
SON	**1**	**0.72**	**0.74**	0.47
SON	**2**	**0.71**	**0.83**	**0.65**
JFM	**1**	**0.91**	**0.92**	**0.95**
MAM	**1**	**0.94**	**0.97**	**0.96**

Table 4: Correlation between the SST PC associated with rotated EOF mode n and the time series associated with optimal pattern n of 200 hPa height for each of the three GCMs. Numbers in bold are significant at the 99% level.

Appendix. Optimizing Signal-to-Noise Denoting the variable X at grid point i, time n, where $1 \leq n \leq N$, and for ensemble member m, where $1 \leq m \leq M$, as X_{inm}, we consider an expansion of X in terms of a set of patterns P and their associated time series α:

$$X_{inm} = \sum_r P_i^r \alpha_{nm}^r \tag{1}$$

where the index r denotes the mode, or pattern. The only prior constraint we place on this expansion is that the time serie α be derivable from a linear transformation of the original data:

$$\alpha_{nm}^r = \sum_i e_i^r X_{inm} \tag{2}$$

Define the ensemble average with an overbar

$$\overline{A}_n = \frac{1}{M} \sum_m A_{nm} \tag{3}$$

and the time average with square brackets

$$[A]_m = \frac{1}{N} \sum_n A_{nm} \tag{4}$$

Assuming that the climate (ensemble time mean) has been removed, so that

$$\left[\overline{X_{inm}}\right] = 0 \tag{5}$$

for all i, we also then have:

$$[\overline{\alpha_{nm}^r}] = [\overline{\alpha}_n^r] = 0 \tag{6}$$

The *signal* S and *noise* N are defined in terms of the time series of a particular mode, or pattern:

$$\mathcal{S} = \left[(\overline{\alpha}_n^r)^2\right] \tag{7}$$

and

$$\mathcal{N} = \left[\overline{(\alpha_{nm}^r - \overline{\alpha}_n^r)^2}\right] \tag{8}$$

Temporarily omitting the pattern index r, and considering the rth column of e_i^r to be a vector e_i, we can write

$$\mathcal{S} = \left[\left(\sum_i e_i \overline{X}_{in}\right)^2\right] = \left[\left(\sum_i e_i \overline{X}_{in} \sum_j e_j \overline{X}_{jn}\right)\right] = \sum_i \sum_j e_i \left(\left[\overline{X}_{in}\overline{X}_{jn}\right]\right) e_j \tag{9}$$

Defining

$$A_{ij} = \left[\overline{X}_{in}\overline{X}_{jn}\right] \tag{10}$$

as the (square symmetric and positive definite) covariance matrix of the ensemble means, the signal becomes:

$$\mathcal{S} = \sum_i e_i A_{ij} e_j = \boldsymbol{e^T} \cdot \boldsymbol{A} \cdot \boldsymbol{e} \tag{11}$$

where lower (upper) case bold letters are used to refer to vectors (matrices), and the superscript T denotes matrix transpose.

In a similar way, using equation 2, the noise can be written as:

$$\mathcal{N} = \left[\overline{\left(\sum_i e_i(X_{inm} - \overline{X}_{in})\right)^2}\right] = \frac{1}{N}\sum_n \overline{\left(\sum_i e_i X'_{inm}\right)^2} \tag{12}$$

where we have defined the primes to denote the noise, that is, the deviations about the ensemble mean:

$$X'_{inm} = X_{inm} - \overline{X}_{in} \tag{13}$$

There is a relationship giving the time series of the noise in terms of the original data, derived from 2 by subtracting the ensemble mean:

$$\alpha'^r_{nm} = \sum_i e_i^r X'_{inm} \tag{14}$$

Similar to the development following equation 9 we can write the noise as:

$$\mathcal{N} = \sum_i e_i B_{ij} e_j = \boldsymbol{e^T \cdot B \cdot e} \tag{15}$$

where B_{ij} is the square symmetric and positive definite covariance matrix of deviations about the ensemble mean:

$$B_{ij} = \left[\overline{X'_{inm} X'_{jnm}}\right] \tag{16}$$

Now the signal to noise ratio $\mathcal{R} = \mathcal{S}/\mathcal{N}$ just

$$\mathcal{R} = \frac{\boldsymbol{e^T \cdot A \cdot e}}{\boldsymbol{e^T \cdot B \cdot e}} \tag{17}$$

The denominator can be diagnolized utilizing the vector $\boldsymbol{g}$ which is defined as

$$\boldsymbol{g} = \boldsymbol{B^{1/2}} \cdot \boldsymbol{e} \tag{18}$$

or

$$\boldsymbol{e} = \boldsymbol{B^{-1/2}} \cdot \boldsymbol{g} \tag{19}$$

Note that the matrix $\boldsymbol{B^{1/2}}$ and its inverse are also square symmetric (and positive definite) matrices. Using equation 19 it is straightforward to show that the ratio $\mathcal{R}$ can be written as:

$$\mathcal{R} = \frac{\boldsymbol{g^T} \cdot \boldsymbol{C} \cdot \boldsymbol{g}}{\boldsymbol{g^T} \cdot \boldsymbol{g}} \tag{20}$$

where the (square symmetric and positive definite) matrix $\boldsymbol{C}$ is defined as:

$$\boldsymbol{C} = \left(\boldsymbol{B^{-1/2}}\right)^{\boldsymbol{T}} \cdot \boldsymbol{A} \cdot \boldsymbol{B^{-1/2}} \tag{21}$$

Equation 20 is of Rayleigh quotient form. By the Rayleigh quotient theorem, the maximum varue of $\mathcal{R}$ is the maximum eigenvalue of $\boldsymbol{C}$, and this maximum is obtained when $\boldsymbol{g}$ equals the corresponding eigenvector. The eigenvectors are orthogonal:

$$\left(\boldsymbol{g^r}\right)^{\boldsymbol{T}} \cdot \boldsymbol{g^s} \ = \delta_{r,s} \tag{22}$$

which becomes, using equation 18:

$$\left(\boldsymbol{e^r}\right)^{\boldsymbol{T}} \cdot \boldsymbol{B} \cdot \boldsymbol{e^s} \ = \delta_{r,s} \tag{23}$$

In these equations r and s refer to modes in the eigenvector expansion. This can be further written, using equation 16 as:

$$\sum_i \sum_j e_i^r B_{ij} e_j^s = \sum_i \sum_j e_i^r \left[\overline{X'_{inm} X'_{jnm}}\right] e_j^s = \left[\overline{\alpha'^r_{nm} \alpha'^s_{nm}}\right] = \delta_{r,s} \tag{24}$$

where we have used equation 14.

The set of modes derived from this eigenvalue/eigenvector problem are identified as the modes which optimize the signal to noise ratio R. Through equations 19, 1, 2 and 14, these modes define the optimal patterns $\boldsymbol{P^r}$ and the corresponding time series for the signal and noise ($\overline{\alpha}_n^r$ and α'^r_{nm}). Note that the patterns $\boldsymbol{P^r}$ are called the *physical* patterns, and the patterns $\boldsymbol{e^r}$ used to derive the time series are called the *filter patterns*. From equation 24 we see that the noise time series corresponding to different modes are independent.

The physical pattern P_i^r can be obtained directly by writing the version of equation 1 for the noise:

$$X'_{inm} = \sum_r P_i^r \alpha'^r_{nm} \tag{25}$$

Multiplying this equation by α'^s_{nm}, averaging over time and ensemble members, and using equation 24 we obtain:

$$\left[\overline{\alpha'^s_{nm} X'_{inm}}\right] = \sum_r P_i^r \left[\overline{\alpha'^s_{nm} \alpha'^r_{nm}}\right] = P_i^s \tag{26}$$

But from equation 14 for mode s

$$\alpha'^s_{nm} = \sum_j e_j^s X'_{jnm} \tag{27}$$

so that:

$$P_i^s = \sum_j e_j^s \left[\overline{X'_{jnm} X'_{inm}}\right] = \sum_j e_j^s B_{ij} \tag{28}$$

When multiplied by e_i^r and summed over i, this gives (using equation 24):

$$\sum_i e_i^r P_i^s = \delta_{r,s} \tag{29}$$

showing that the physical and filter patterns form a bi-orthogonal set.

In practice, the fields X_{inm} are represented in terms of an EOF expansion to carry out these calculations. We retained 10 EOF patterns for each GCM.

References

Branković, C. and T. N. Palmer, 1997: Atmospheric seasonal predictability and estimates of ensemble size. *Mon. Wea. Rev.,* **125**, 859–874.

Branković, C. and T. N. Palmer, 2000: Seasonal skill and predictability of ecmwf provost ensembles. *Quart. J. Roy. Meteor. Soc.,* **126**, 2035–2067.

Chang, Y., S. D. Schubert, and M. J. Suarez, 2000: Boreal winter predictions with the GEOS-2 GCM: The role of boundary focing and initial conditions. *Quart. J. Roy. Meteor. Soc.,* **126**, 2293–2323.

Hoerling, M. P., A. Kumar, and T. Xu, 2001: Robustness of the nonlinear climate response to ENSO's extreme phases. *J. Climate,* **14**, 1277–1293.

Hoerling, M. P., M. Ting, and A. Kumar, 1995: Zonal flow-stationary wave relationship during El-Niño: Implications for seasonal forecasting. *J. Climate,* **8**, 1838–1852.

Kalnay, E. and coauthors, 1996: The NCEP/NCAR 40-year reanalysis project. *Bull. Amer. Meteor. Soc.,* **77**, 437–472.

Kanamitsu, M., A. Kumar, H.-M. H. Juang, J.-K. Schemm, W. Wang, F. Yang, S.-Y. Hong, P. Peng, W. Chen, S. Morthi, and M. Ji, 2002: NCEP dynamical seasonal forecast system 2000. *Bull. Amer. Meteor. Soc.,* **83**, 1019–1037.

Kiehl, J. T., J. J. Hack, G. Bonan, B. A. Boville, D. L. Williamson, and P. J. Rasch, 1998: The National Center for Atmospheric Research Community Climate Model: CCM3. *J. Climate,* **11**, 1131–1149.

Koster, R. D. and M. J. Suarez, 1992: A comparative analysis of two land surface heterogeneity representations. *J. Climate,* **5**, 1379–1390.

Kumar, A., A. G. Barnston, P. Peng, M. P. Hoerling, and L. Goddard, 2000: Changes in the spread of the variability of the seasonal mean atmospheric states associated with ENSO. *J. Climate,* **13**, 3139–3151.

Kumar, A. and M. P. Hoerling, 1998: Annual cycle of pacific-north american seasonal predictability associated with different phases of ENSO. *J. Climate,* **11**, 3295–3308.

Livezey, R. E., M. Masutani, A. Leetmaa, H. Rui, M. Ji, and A. Kumar, 1997: Teleconnective response of the pacific-north american region atmosphere to large central equatorial pacific sst anomalies. *J. Climate,* **10**, 1787–1820.

Moorthi, S. and M. J. Suarez, 1992: A parameterization of moist convection for general circulation models. *Mon. Wea. Rev.,* **210**, 978–1002.

Pan, H.-L. and L. Mahrt, 1987: Interaction between soil hydrology and boundary layer developments. *Bound.-Layer Meteor.,* **38**, 185–202.

Reynolds, R. W. and T. M. Smith, 1994: Improved global sea surface temperature analyses using optimal interpolation. *J. Climate,* **9**, 840–858.

Rowell, D. P., C. K. Folland, K. Maskell, and M. N. Ward, 1995: Variability in summer rainfall over tropical North Africa (1906-92): Observations and modelling. *Quart. J. Royal Meteor. Soc.,* **121**, 669–704.

Scheffé, H., 1959. *The Analysis of Variance.* New York: John Wiley & Sons, Inc.

Schneider, E. K., 2002: Understanding differences between the equatorial pacific as simulated by two coupled gcms. *J. Climate,* **15**, 449–469.

Schubert, S. D., M. J. Suarez, Y. Chang, and G. Branstator, 2001: The impact of ENSO on extratropical low-frequency noise in seasonal forecasts. *J. Climate,* **14**, 2351–2365.

Schubert, S. D., M. J. Suarez, P. J. Pegion, M. A. Kistler, and A. Kumar, 2002: Predictability of zonal means during boreal summer. *J. Climate,* **15**, 420–434.

Shukla, J., J. Anderson, D. Baumhefner, C. Brankovic, Y. Chang, E. Kalnay, L. Marx, T. Palmer, D. Paolino, J. Ploshay, Schubert, D. Straus, M. Suarez, and J. Tribbia, 2000a: Dynamical seasonal prediction. *Bull. Amer. Meteor. Soc.,* **81**, 2593–2606.

Shukla, J., D. A. Paolino, D. M. Straus, D. DeWitt, M. Fennessy, J. L. Kinter, L. Marx, and R. Mo, 2000b: Dynamical seasonal prediction with the COLA atmospheric model. *Quart. J. Roy. Meteor. Soc.,* **126**, 2265–2291.

Smith, T. M., R. W. Reynolds, R. E. Livezey, and D. C. Stokes, 1996: Reconstruction of historical sea surface temperatures using empirical orthogonal functions. *J. Climate,* **9**, 1403–1420.

Straus, D. M. and J. Shukla, 2000: Distinguishing between the SST-forced variability and internal variability in mid latitudes:Analaysis of observations and GCM simulations. *Quart. J. Roy. Meteor. Soc.,* **126**, 2323–2350.

Straus, D. M. and J. Shukla, 2002: Does ENSO force the PNA? *J. Climate,* **128**, 2340–2358.

Venzke, S., M. R. Allen, R. T. Sutton, and D. P. Rowell, 1999: The atmospheric response over the North Atlantic to decadal changes in sea surface temperature. *J. Climate,* **12**, 2562–2584.

Xie, P. and P. A. Arkin, 1997: Global precipitation: A 17-year monthly analysis based on gauge observations, satellite estimates and numerical model outputs. *Bull. Amer. Meteor. Soc.,* **78**, 2359–2558.

Xue, Y.-K., P. J. Sellers, J. L. Kinter, and J. Shukla, 1991: A simplified Biosphere Model for global climate studies. *J. Climate,* **4**, 345–364.

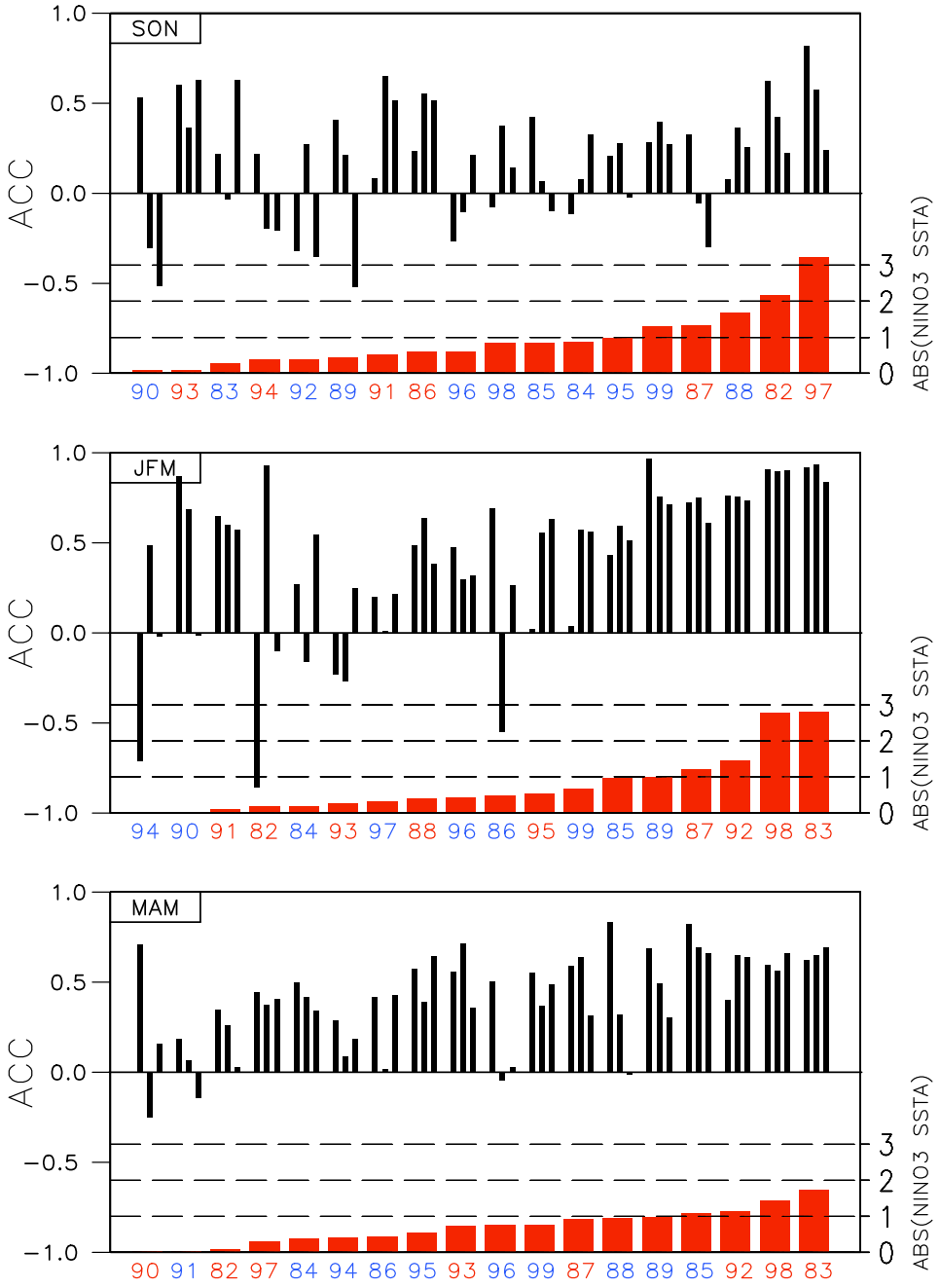

Figure 1: Each thin vertical bar shows the pattern correlation of the ensemble mean seasonal mean 200 hPa height of a GCM with the observed seasonal mean over North America $15^oN - 70^oN$ and $180^oW - 60^oW$.) The pattern correlation is computed separately for each year and for each GCM; the bars show the results for the COLA, NSIPP and NCEP GCMs from left to right. The years are ordered by the absolute value of the Niño-3 index, increasing to the right and shown by the red bars. Red (blue) numbers indicate warm (cold) years. The top panel shows results for boreal autumn (Sept.-Nov.), the middle panel for boreal winter (Jan.-March), the bottom panel for boreal spring (March-May).

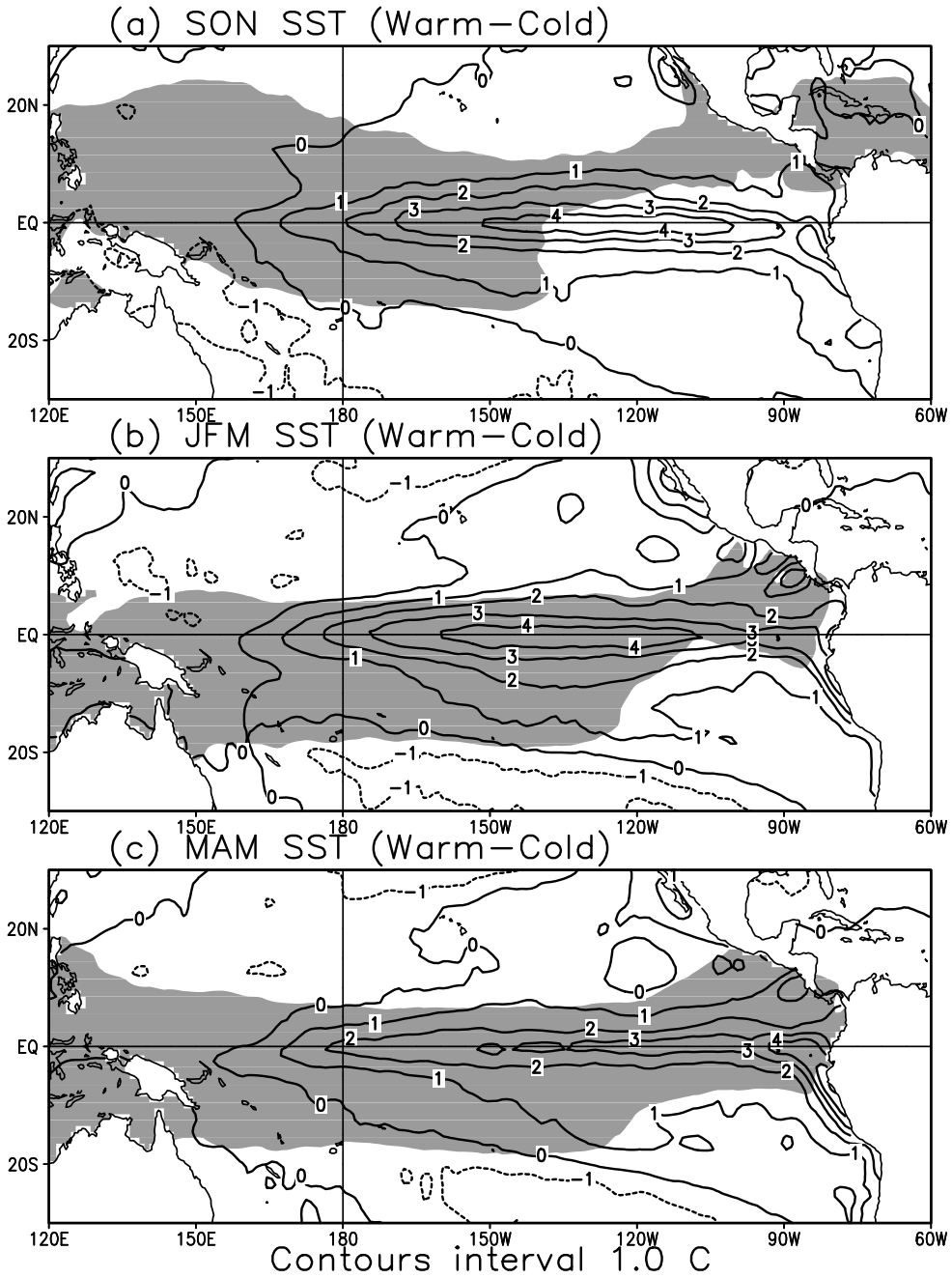

Figure 2: Warm-minus-cold composite seasonal mean SST, in degrees C. Shading indicates regions where the composite warm SST exceeds 28^oK. The warm and cold composites are taken over years based on the value of Niño-3 index for boreal winter; the winter definition applies to the preceding autumn and following spring. See text for details. (a) Autumn, (b) Winter, (c) Spring composite differences.

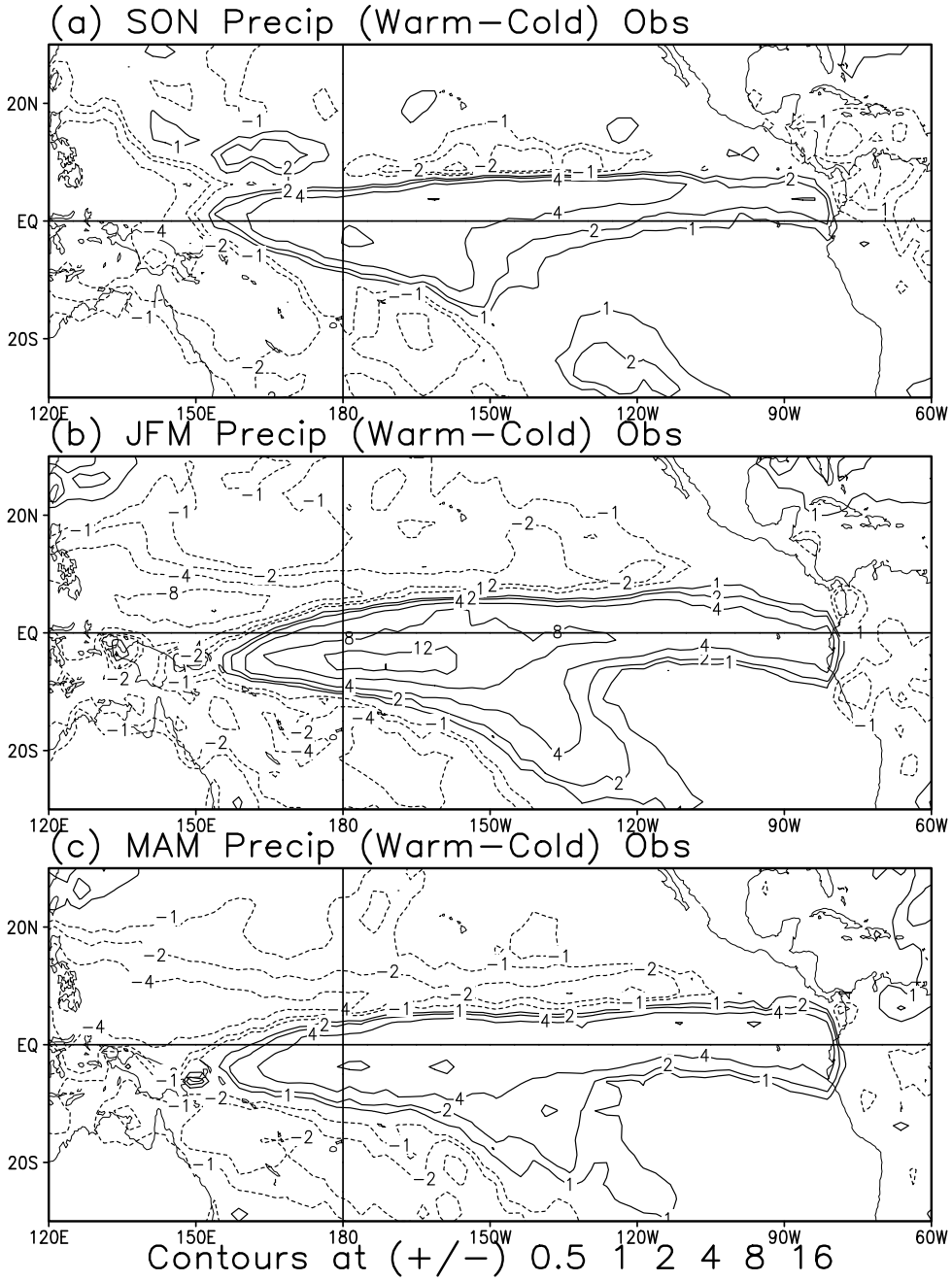

Figure 3: Warm-minus-cold composite seasonal-mean observed precipitation, (Xie and Arkin 1997), in units of mm/day. Contours drawn at $\pm 1, 2, 4, 8, 12, 16$ mm/day. The warm and cold composites are taken over years based on value of Niño3 index for boreal winter; the winter definition applies to the preceding autumn and following spring. See text for details. (a) Autumn, (b) Winter, (c) Spring composite differences.

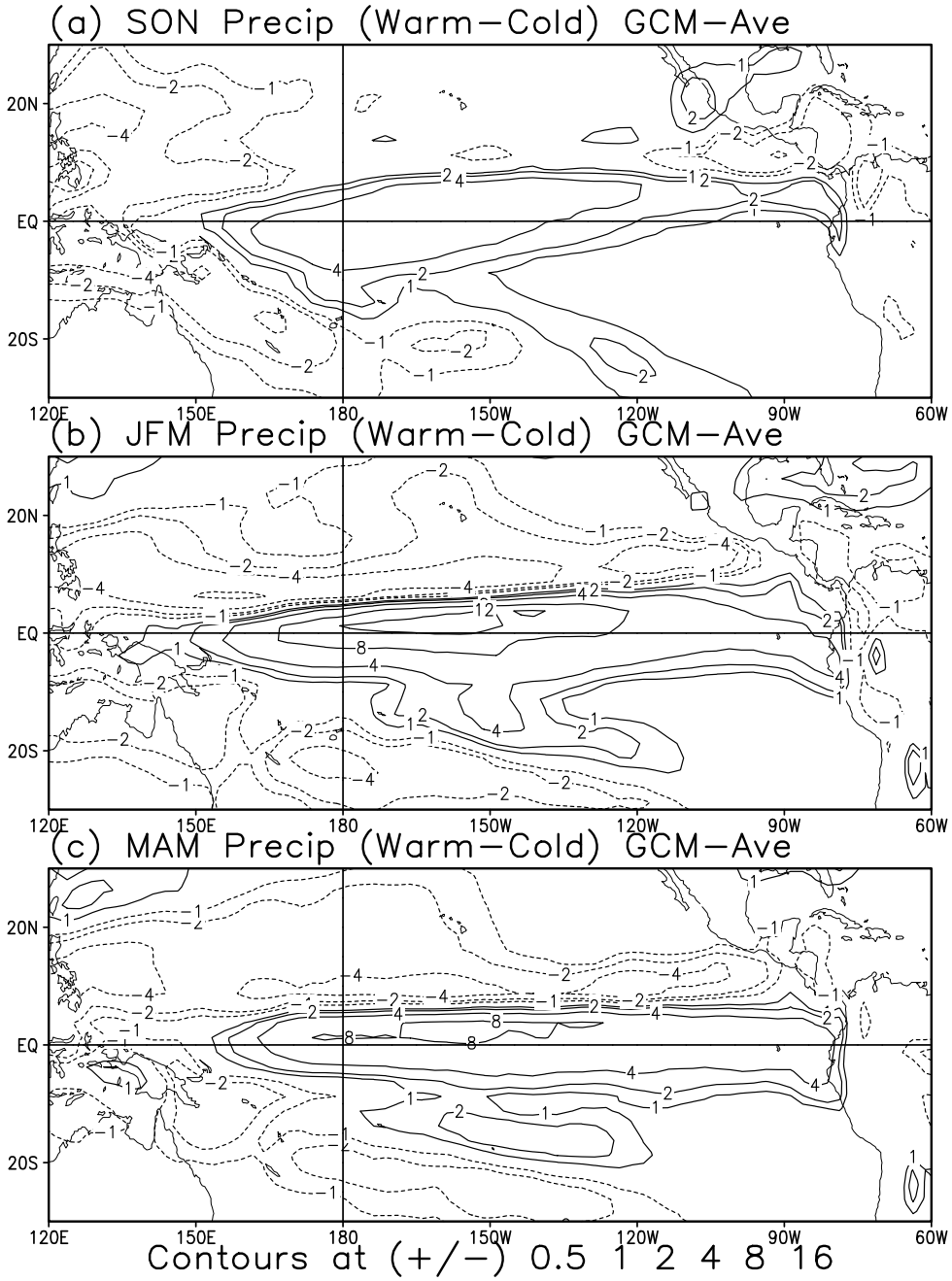

Figure 4: As in Figure 3 except for the average of three GCM ensemble means.

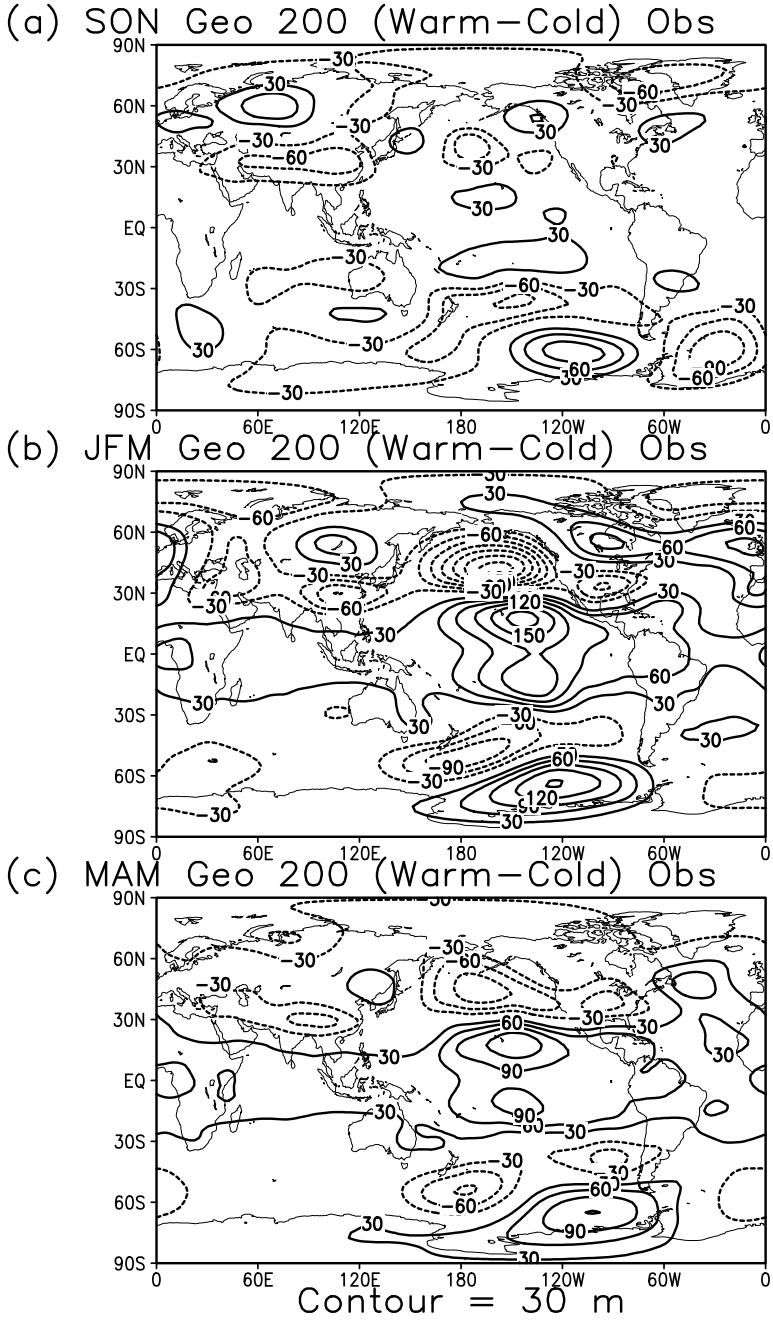

Figure 5: Warm-minus-cold composite seasonal-mean 200 hPa height in units of m. Contour interval is 30m. The warm and cold composites are taken over years based on the value of the Niño-3 index for boreal winter; the winter definition applies to the preceding autumn and following spring. See text for details. (a) Autumn, (b) Winter, (c) Spring composite differences.

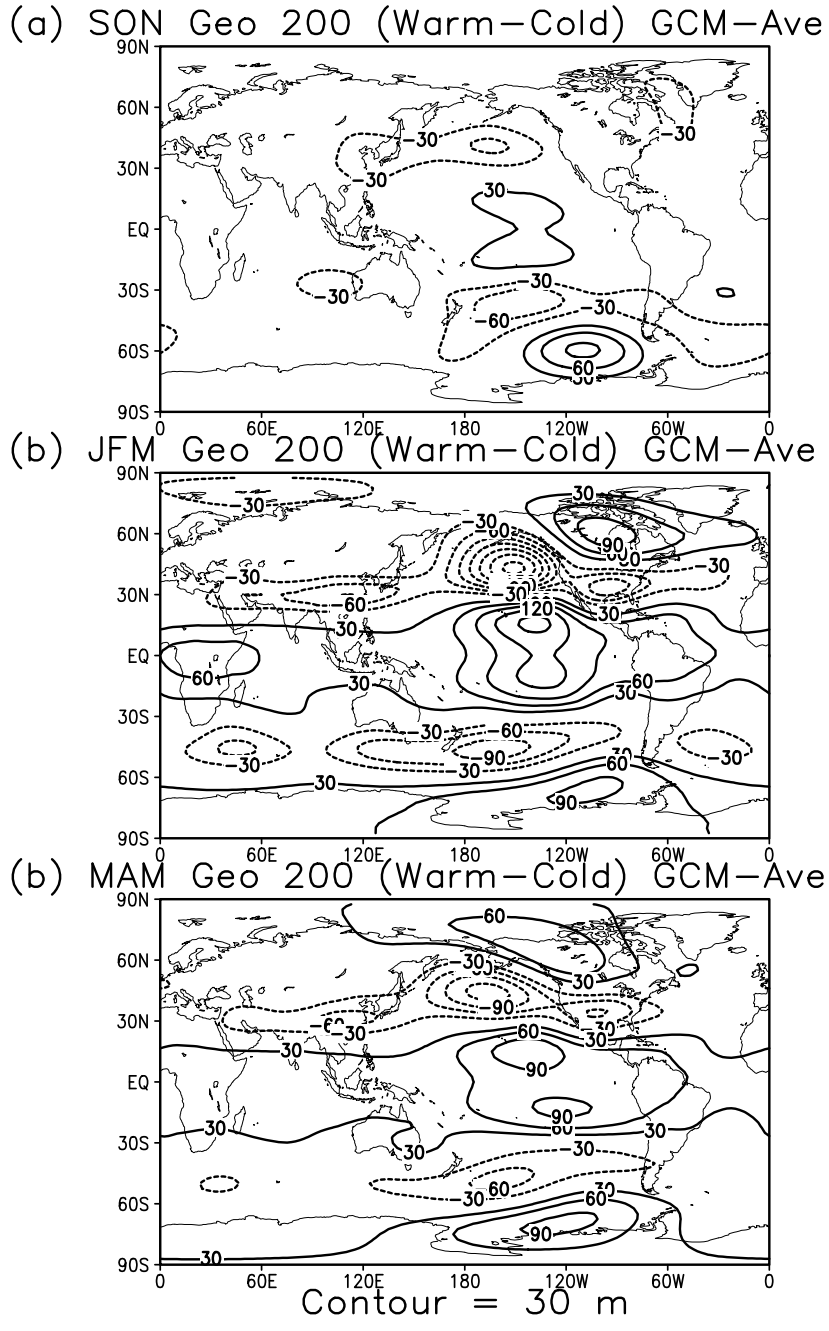

Figure 6: As in Figure 5 except for the average of three GCM ensemble means.

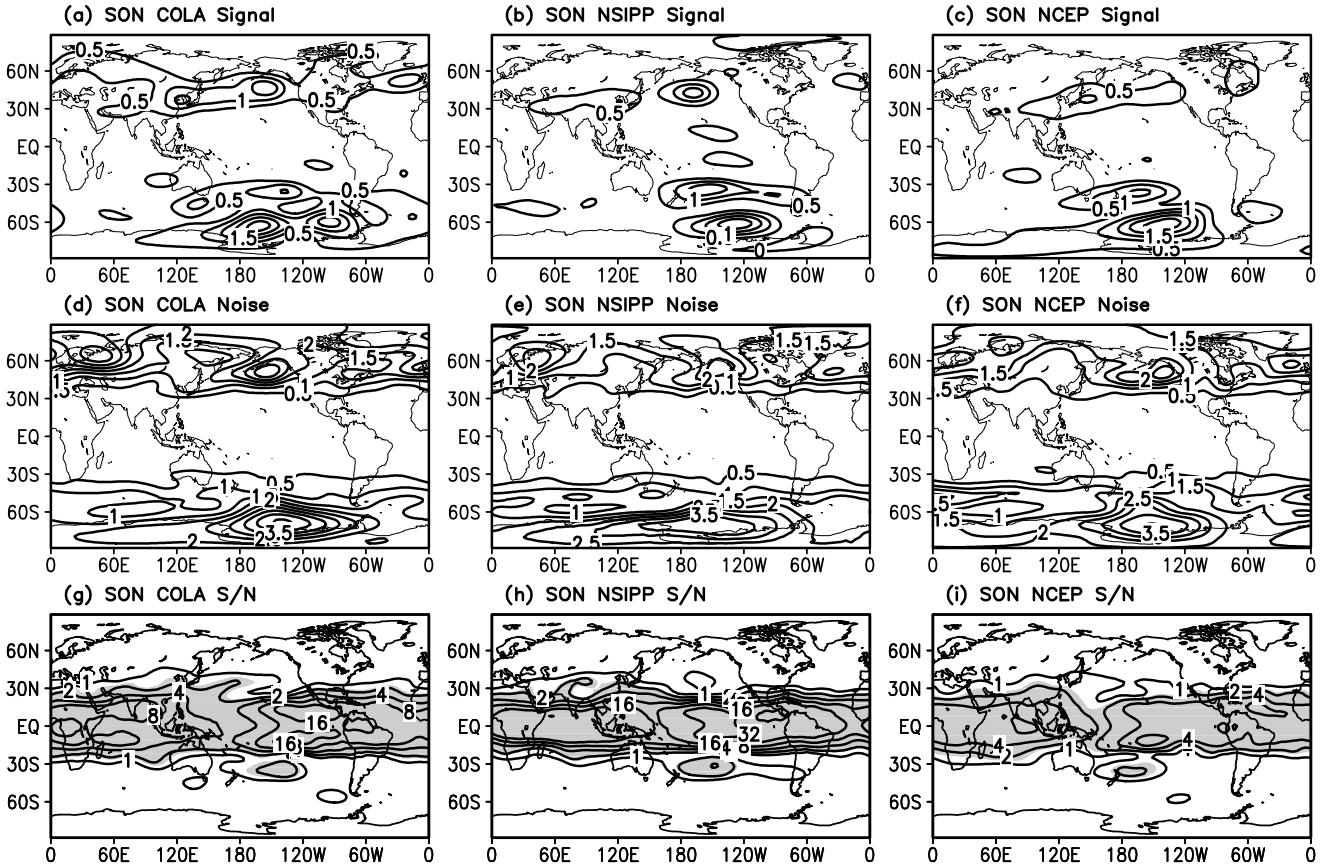

Figure 7: Signal variance (a)-(c), noise variance (d)-(f) and signal-to-noise ratio (g)-(i) for three GCMs for boreal autumn. See text for details. Contour interval is $0.5 \times 10^3 m^2$ in (a)-(f). Dimensionless contours of 1,2,4,8,16,32 and 64 in (g)-(i). Light (dark) shading in (g)-(i) indicates 95% (99%) significance.

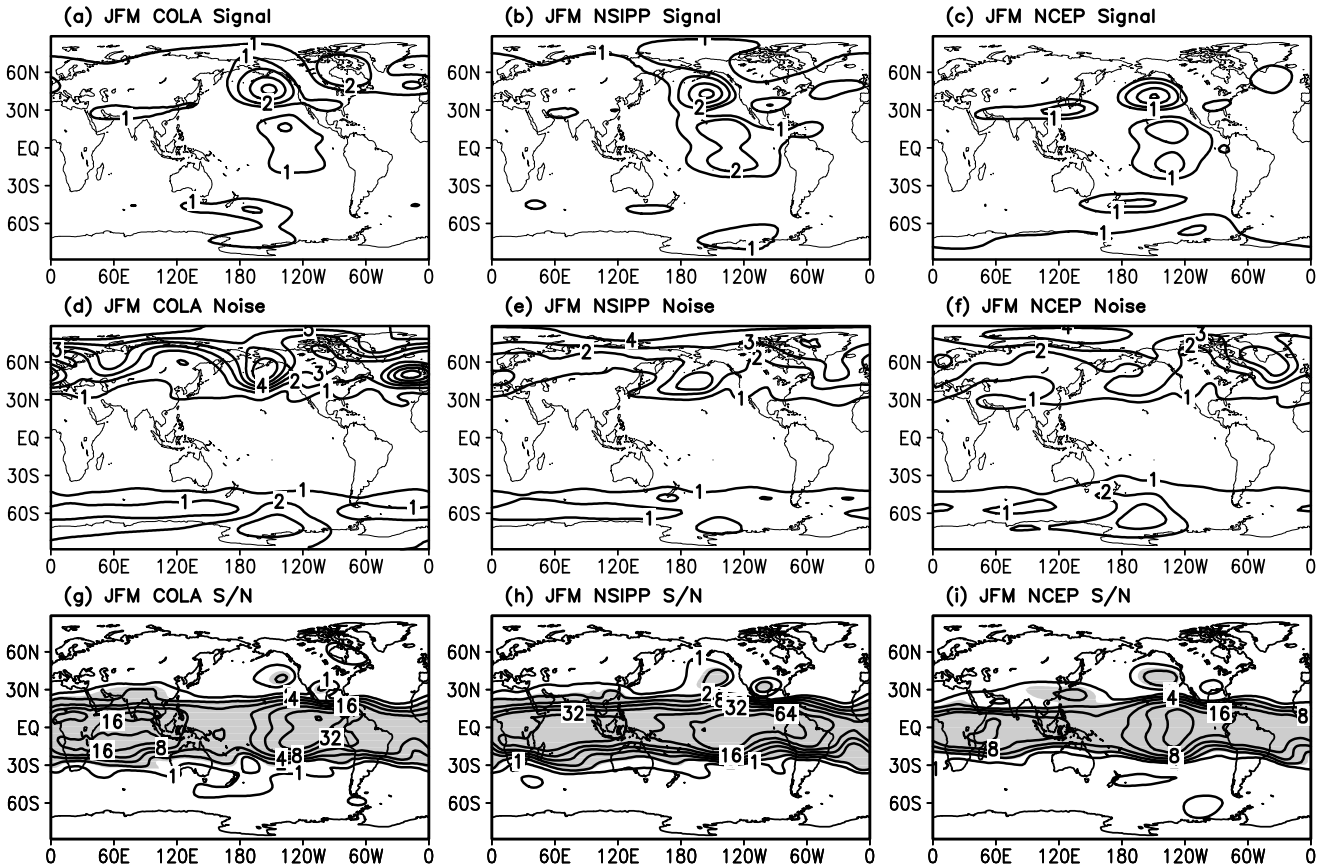

Figure 8: Signal variance (a)-(c), noise variance (d)-(f) and signal-to-noise ratio (g)-(i) for three GCMs for boreal winter. Contour interval is $2.0 \times 10^3 m^2$ in (a)-(c), $1.0 \times 10^3 m^2$ in (d)-(f). Otherwise as in Figure 7.

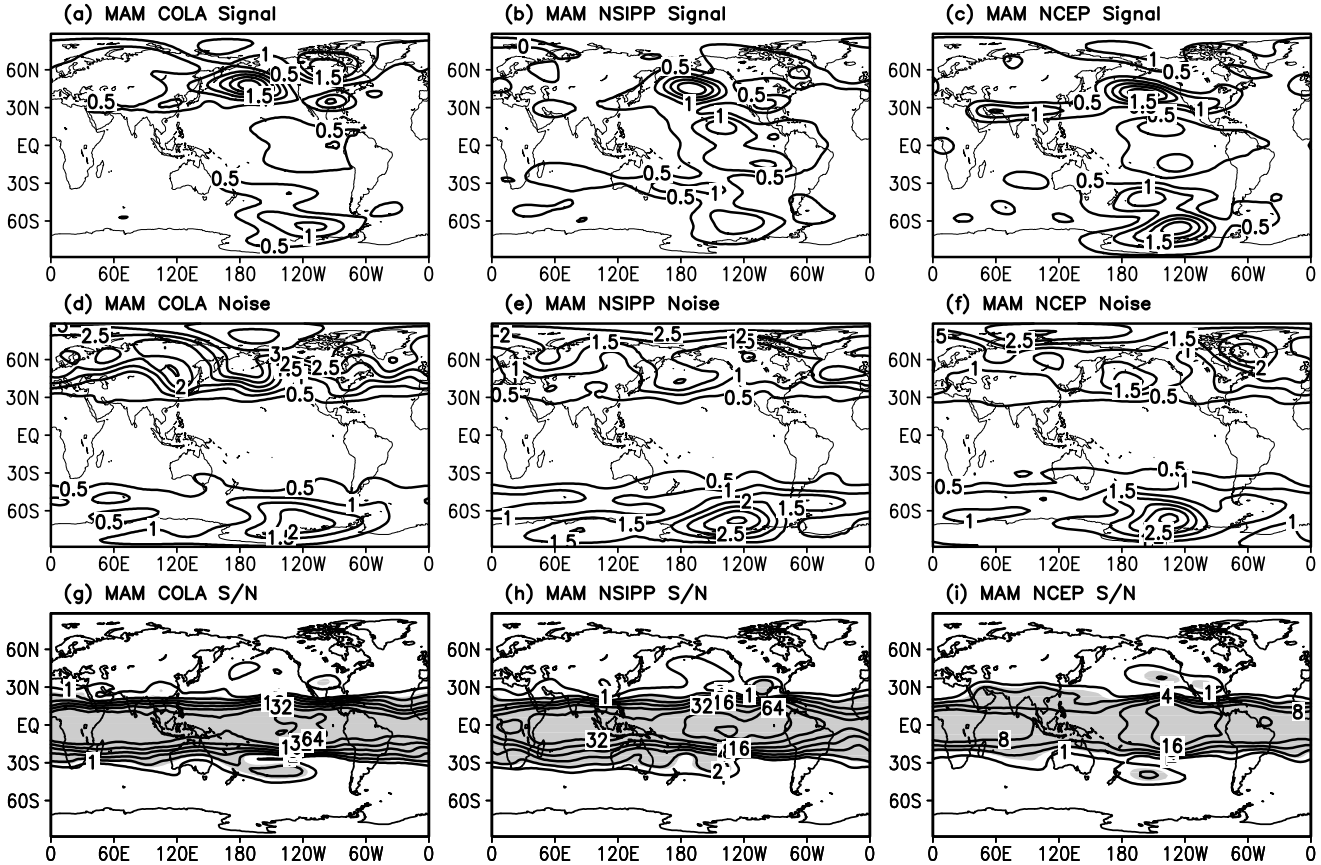

Figure 9: As in 7, but for boreal spring.

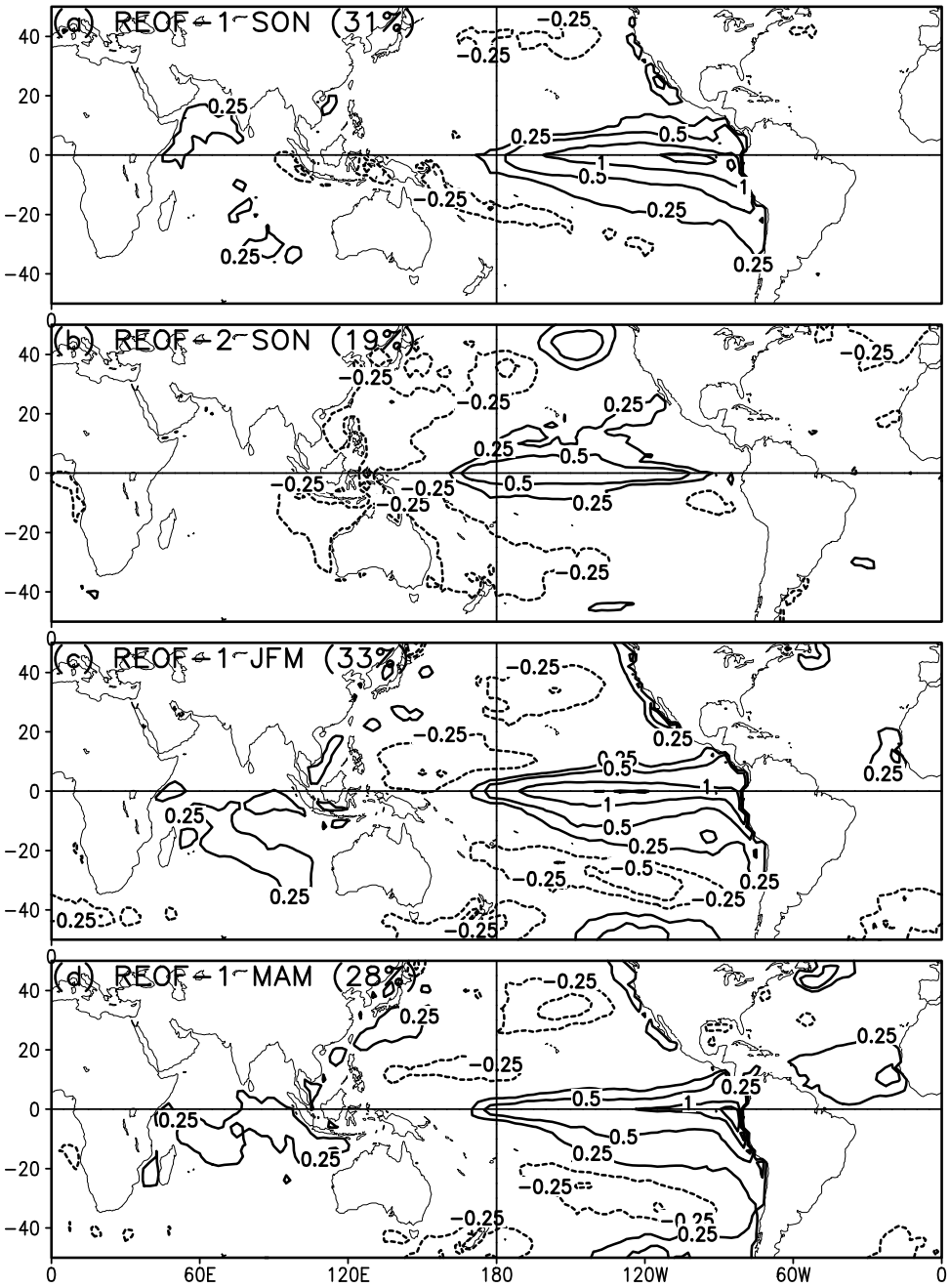

Figure 10: Two leading REOFs of the seasonal mean SST field for boreal autumn (a)-(b); leading REOF for boreal winter (c); for boreal spring (d). Patterns are dimensional, corresponding to the associated time series having unit variance. Contour interval is 0.25 degree C. Percentages in parantheses are explained in the text.

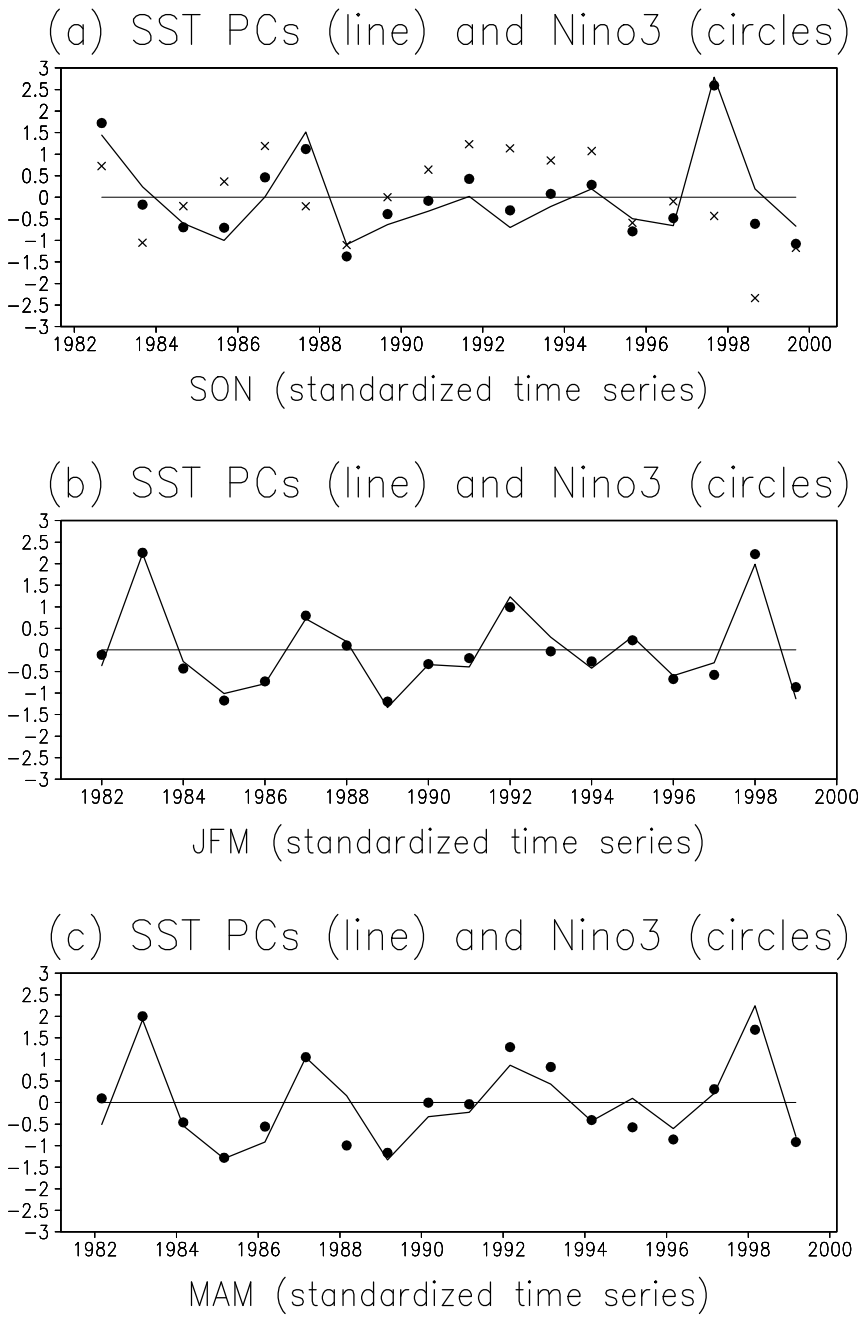

Figure 11: The time series (PCs) associated with the leading REOF patterns of SST shown in Figure 10 are given by the solid lines for boreal autumn, winter and spring in the top, middle and bottom panels. The time series of the Niño-3 index are given by the solid dots. Time series (PC) associated with REOF-2 during autumn are given by the crosses in the top panel. All time series have unit variance.

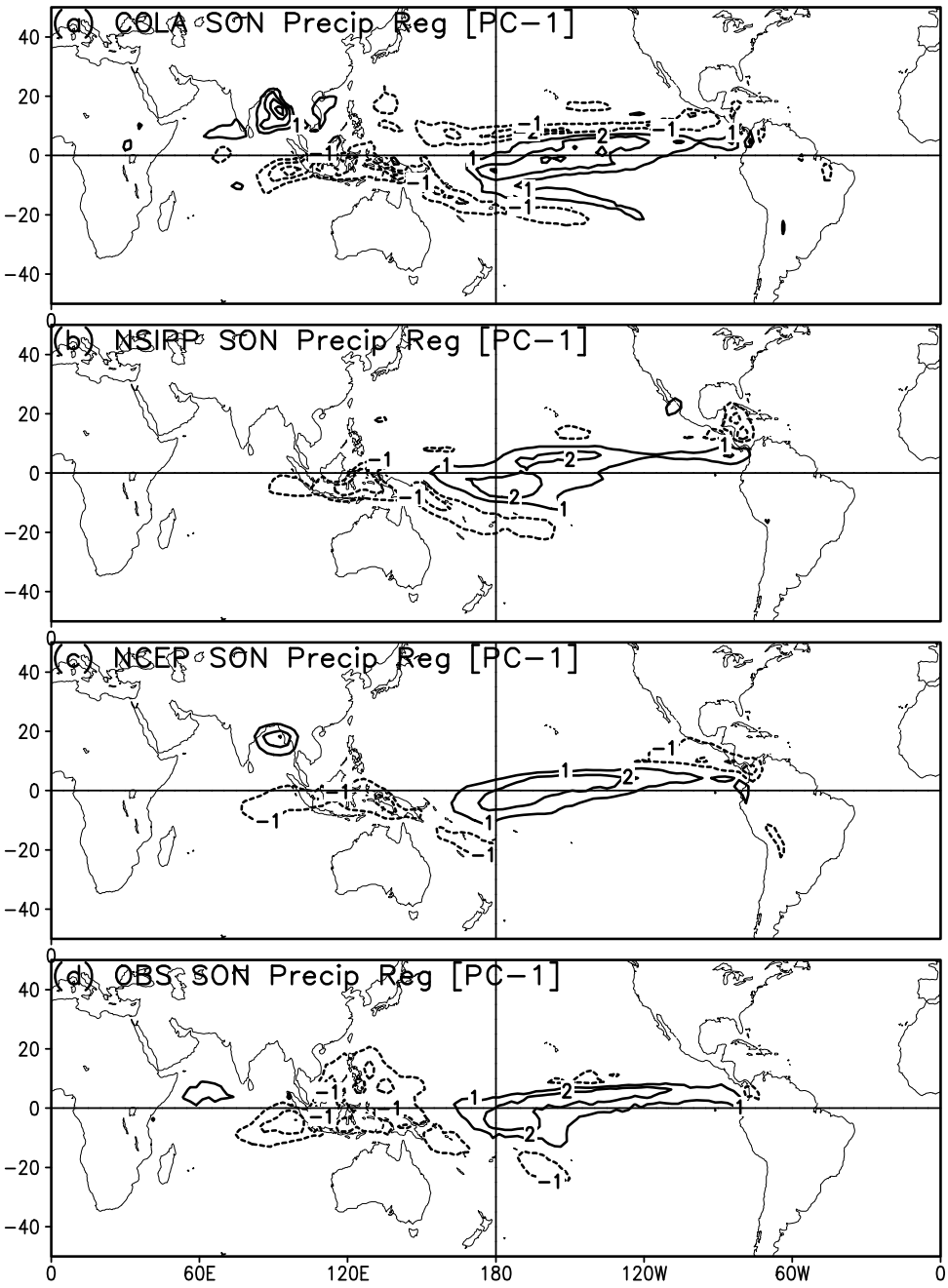

Figure 12: Regression of seasonal-mean precipitation on the PC of the leading REOF of SST for boreal autumn. Top three panels show the regression of the ensemble seasonal mean for the COLA, NSIPP, and NCEP GCMs. Bottom panel shows the regression of observed (Xie and Arkin 1997) precipitation. The regression coefficients have a contour interval of $1\,mm\,day^{-1}C^{-1}$.

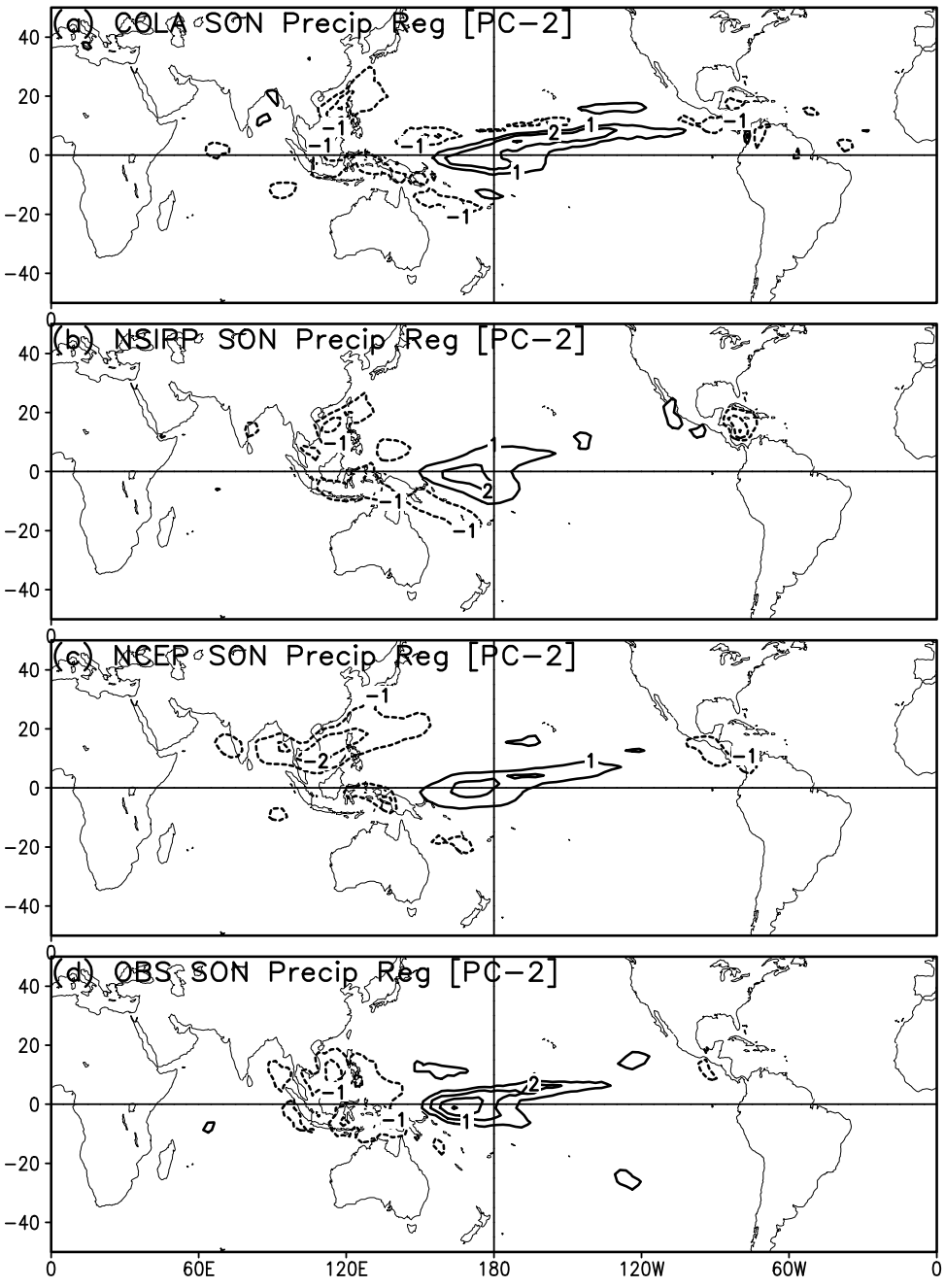

Figure 13: As in Figure 12, but for the second REOF for boreal autumn.

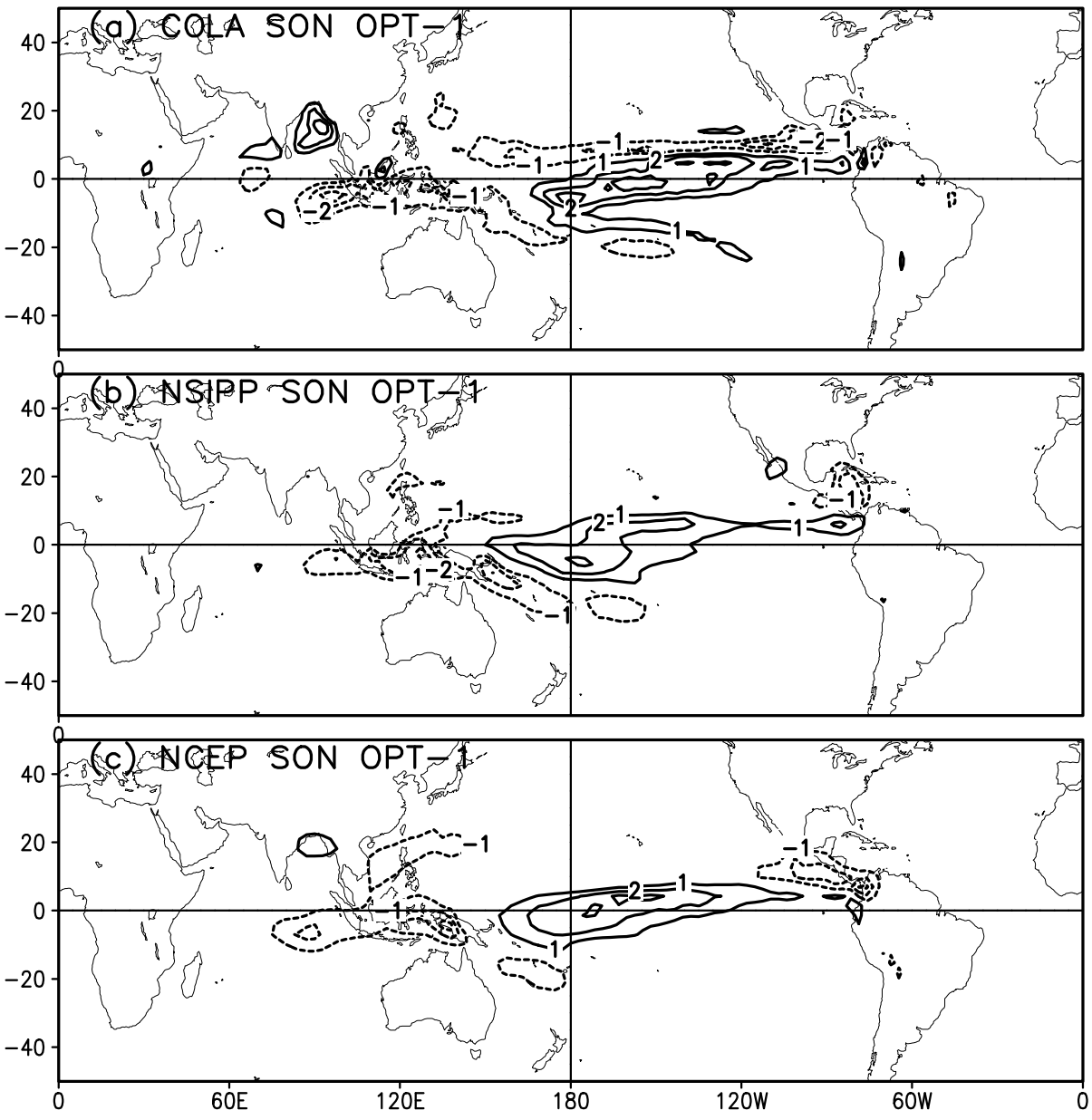

Figure 14: The leading optimal signal-to-noise pattern of precipitation for the COLA, NSIPP, and NCEP GCMs for the boreal autumn. (See text for explanation.) The associated time series have unit variance. Contour interval is 1 $mm\ day^{-1}$.

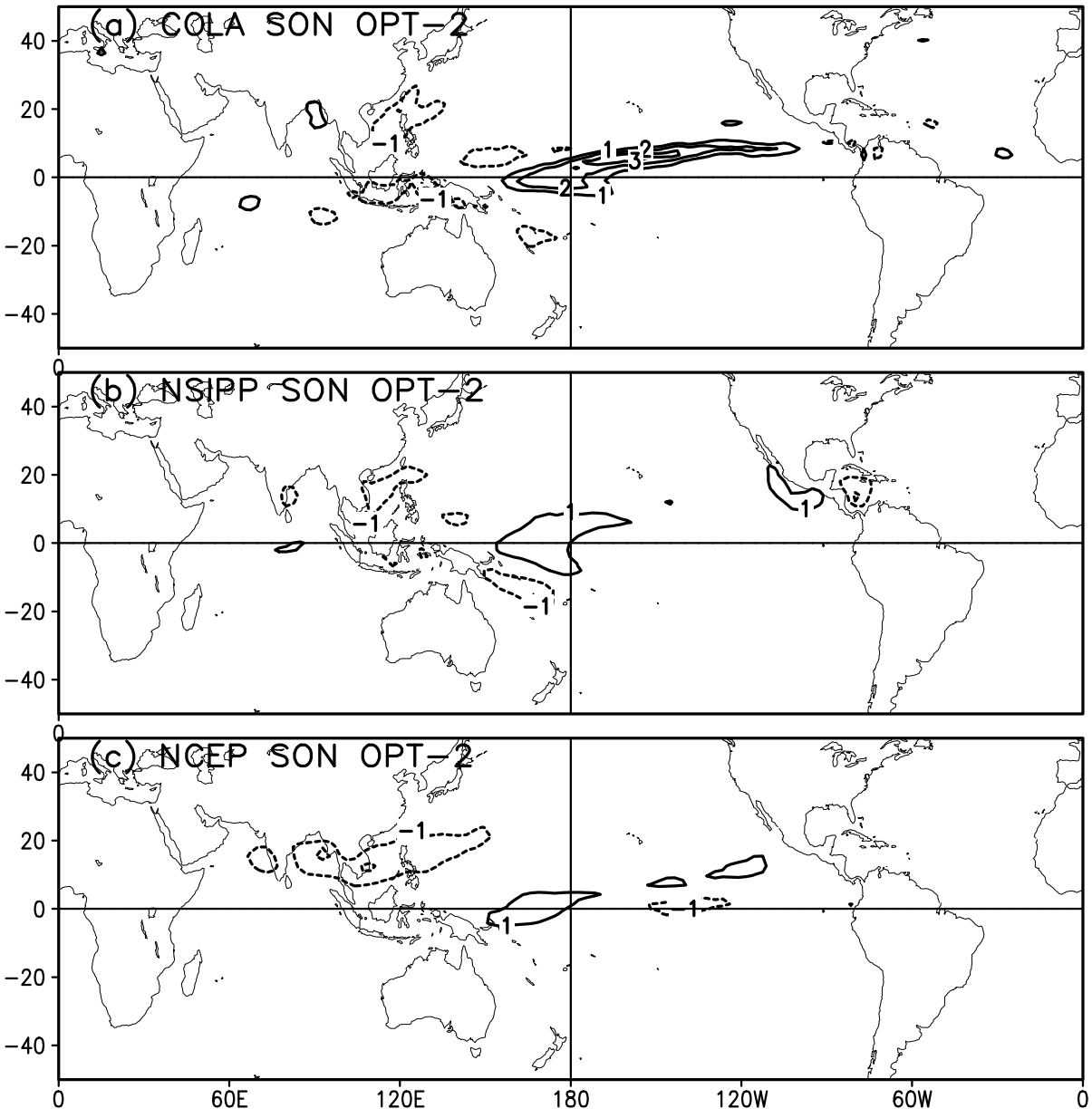

Figure 15: As in Figure 14, but for the second optimal signal-to-noise pattern of precipitation.

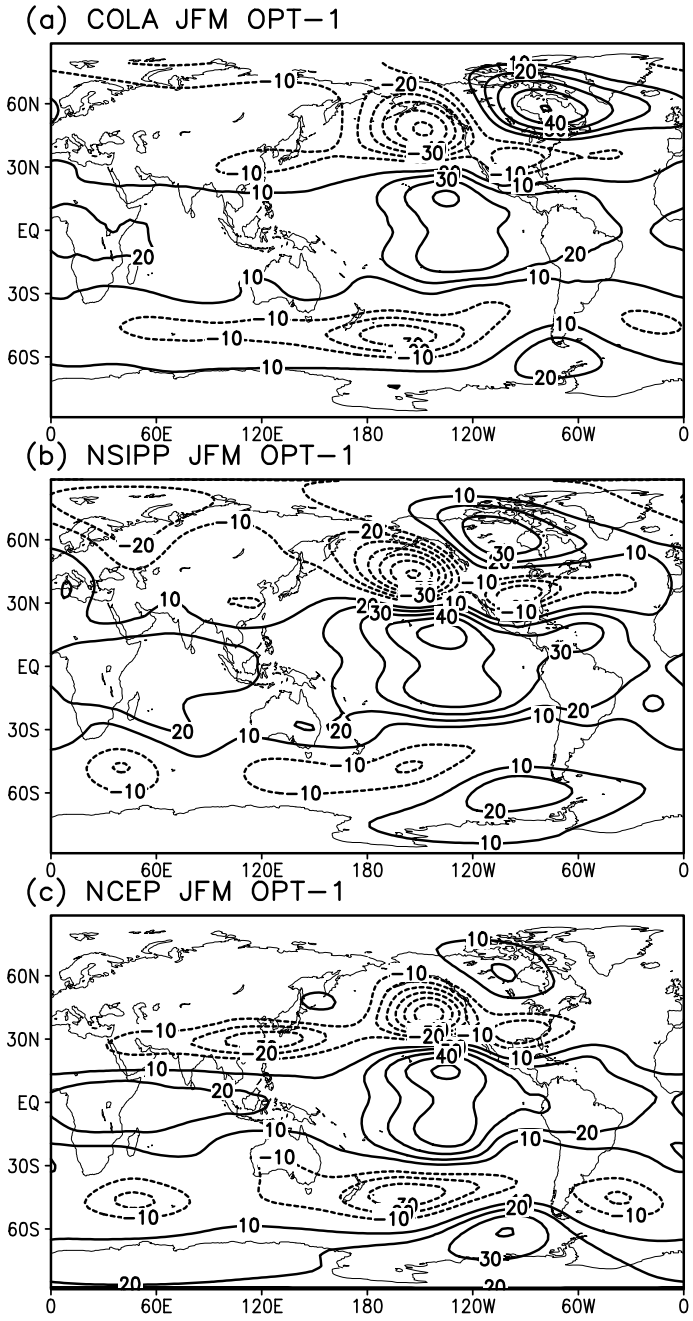

Figure 16: The leading optimal signal-to-noise pattern of 200 hPa height for the COLA, NSIPP, and NCEP GCMs for the boreal winter. (See text for explanation.) The associated time series have unit variance. Contour interval is 10 m.

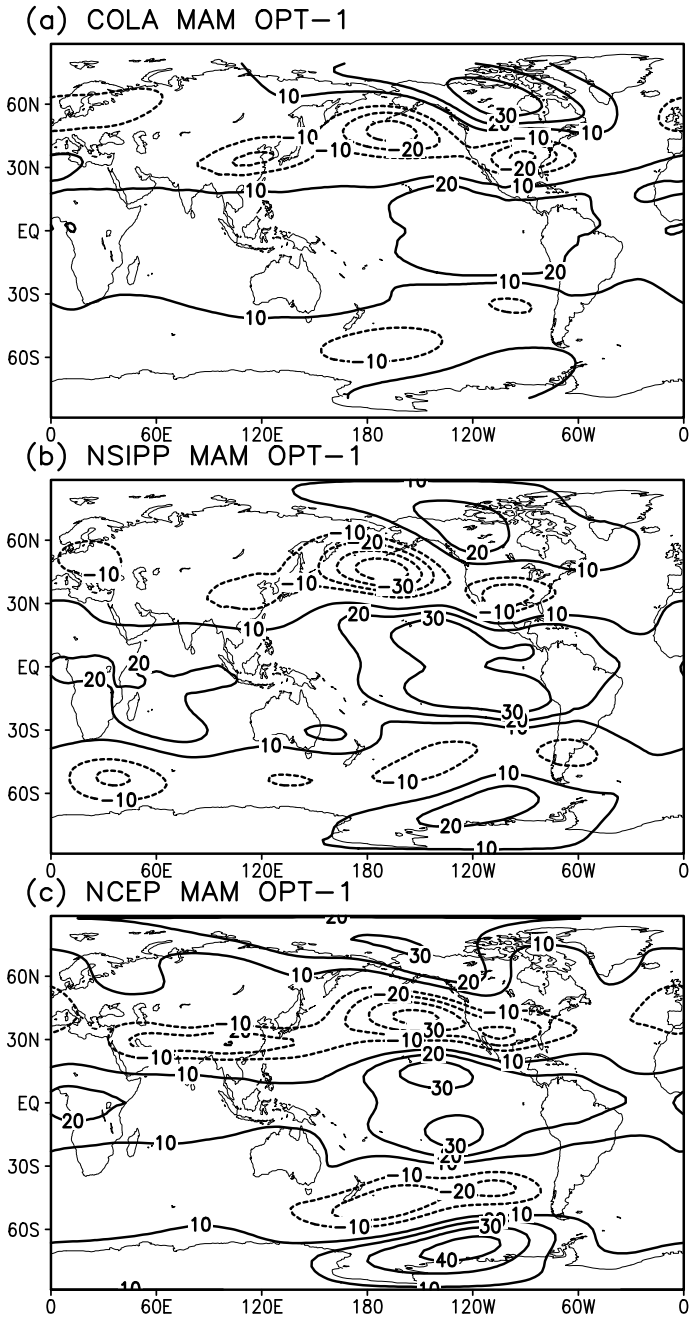

Figure 17: As in Figure 16, but for boreal spring.

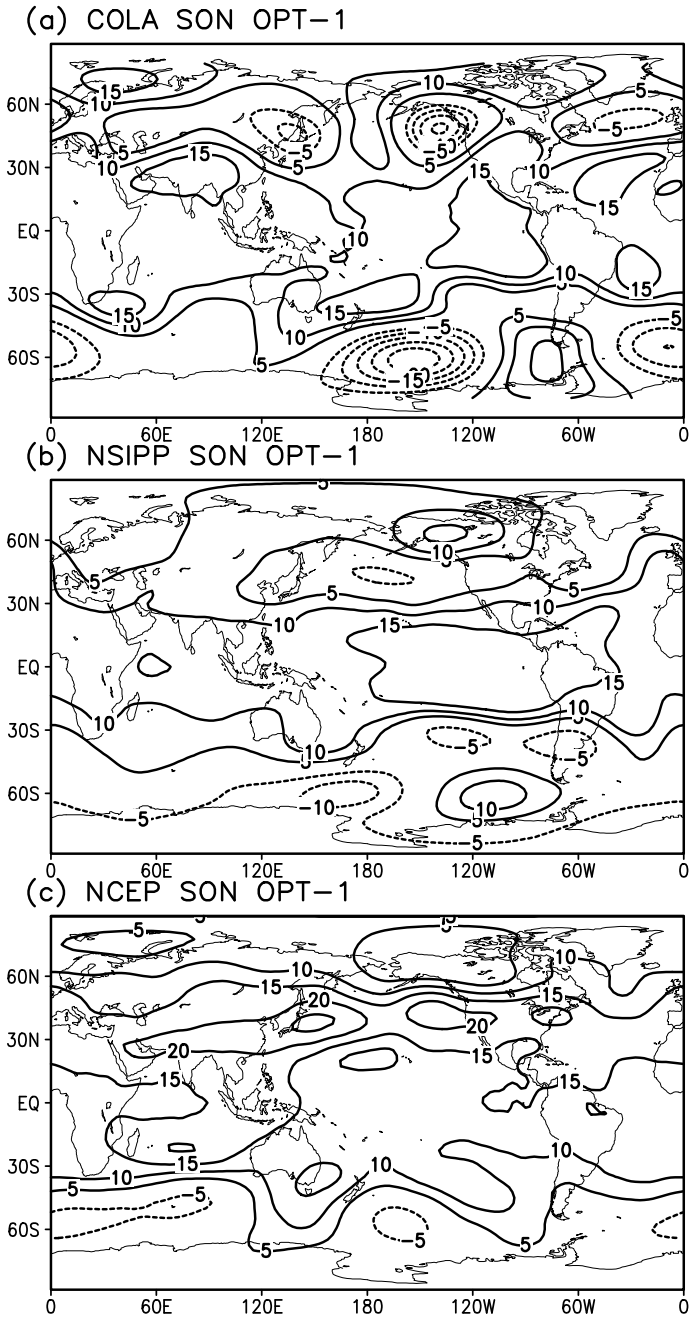

Figure 18: As in Figure 16, but for boreal autumn. Note that the contour interval is 5 m.

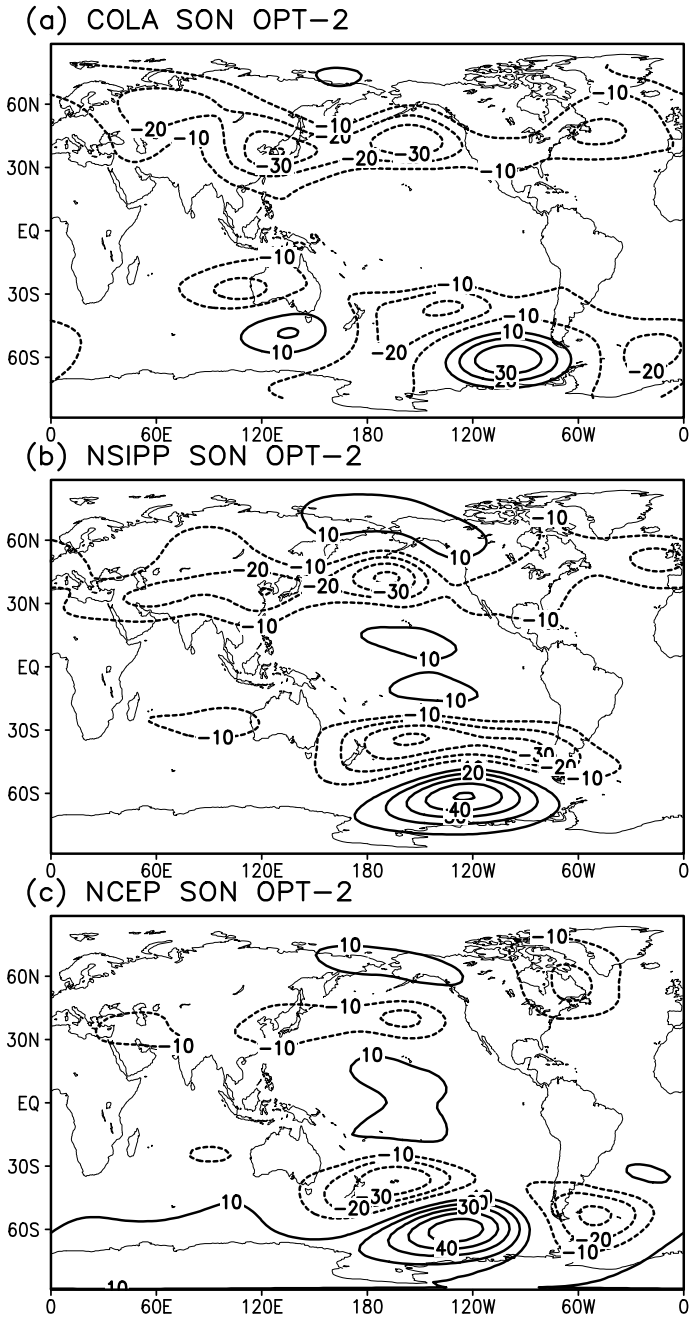

Figure 19: As in Figure 16, but for the second optimal pattern during boreal autumn.